PIEZO1 regulates leader cell formation and cellular coordination during collective keratinocyte migration

Jesse R. Holt* [1,2,3], **Jinghao Chen*** [4], **Elizabeth L. Evans**[1,2], **John S. Lowengrub** † [3,4,5], **Medha M. Pathak** † [1,2,3,5]

[1]Department of Physiology & Biophysics, UC Irvine, Irvine, CA, 92697, USA; [2]Sue and Bill Gross Stem Cell Research Center, UC Irvine, Irvine, CA, 92697, USA; [3]Center for Complex Biological Systems, UC Irvine, Irvine, CA, 92697, USA; [4]Department of Mathematics, UC Irvine, Irvine, CA 92697, USA; [5]Department of Biomedical Engineering, UC Irvine, Irvine, CA, 92697, USA

†**For correspondence:**
medhap@uci.edu (MMP); lowengrb@math.uci.edu (JSL)

*These authors contributed equally to this work

Abstract The collective migration of keratinocytes during wound healing requires both the generation and transmission of mechanical forces for individual cellular locomotion as well as for the coordination of movement across cells. Leader cells initiated along the wound edge transmit mechanical and biochemical cues to ensuing follower cells, ensuring their uniform polarization and coordinated direction of migration, or directionality. Despite the observed importance of mechanical cues in leader cell formation and controlling directionality, the underlying biophysical mechanisms remain elusive. The mechanically activated ion channel PIEZO1 was recently identified to play an inhibitory role during the reepithelialization of wounds through retraction of keratinocytes located along the wound edge. Here, through an integrative experimental and mathematical modeling approach, we elucidate PIEZO1's contributions to collective migration. Time-lapse microscopy reveals that PIEZO1 activity inhibits leader cell formation along the wound edge. To probe the relationship between PIEZO1 activity, leader cell formation and inhibition of reepithelialization, we developed an integrative 2D-multiscale model of wound closure that links observations at the single cell and collective cell migration scales. Through numerical simulations and subsequent experimental validation, we found that directionality plays a key role during wound closure and is inhibited by PIEZO1 activity. We propose that PIEZO1-mediated retraction suppresses leader cell formation which inhibits the coordination of directionality between cells during collective migration.

Introduction

Cell migration plays an essential role in driving a diverse range of physiological processes including embryonic morphogenesis, tissue formation, repair and regeneration (***Franz et al.*** (***2002***); ***Friedl and Gilmour*** (***2009***)). This multistep process of cellular locomotion relies upon the orchestrated coordination between several cellular processes including: actin polymerization, exertion of actomyosin-based contractile forces, and the dynamics of adhesion complexes (***Ridley et al.*** (***2003***)). During single cell migration, cells migrate directionally by becoming polarized. Located at the front of polarized cells, the leading edge drives forward locomotion while the rear, or retracting region, underlies the physical translocation of the cell body (***Seetharaman and Etienne-Manneville*** (***2020***); ***SenGupta et al.*** (***2021***); ***Vicente-Manzanares and Horwitz*** (***2011***)). Under many physiological contexts, cells increase their migration efficiency by migrating together as a multicellular unit. During this collective form of cell migration, cells locomote while maintaining cell-cell contacts thus enabling subpopulations of cells to move interdependently (***Mayor and Etienne-Manneville*** (***2016***); ***Weijer*** (***2009***)). In addition to each cell polarizing individually, collectively migrating populations of cells become uniformly polarized due to the communication of mechanical and biochemical information through cell-cell contacts (***Capuana et al.*** (***2020***); ***Venhuizen and Zegers*** (***2017***)). This multicellular polarization is initiated by specialized cells, termed leader cells, located at the front of groups of collectively migrating cells (***Poujade et al.*** (***2007***)). Through the local coordination of intracellular mechanical forces, leader cells dictate the speed and the directionality of follower cells located behind them (***Angelini et al.*** (***2011***); ***Cai et al.*** (***2014***); ***Das et al.*** (***2015***); ***Deforet et al.*** (***2014***); ***Doxzen et al.*** (***2013***); ***Ladoux and Mège*** (***2017***); ***Tambe et al.*** (***2011***); ***Trepat et al.*** (***2009***)). This large-scale polarization and coordination of motion by leader cells is able to span across multiple cells, covering hundreds of micrometers in length (***Angelini et al.*** (***2010***); ***Petitjean et al.*** (***2010***)). Thus the collective behaviors and dynamics of migrating sheets of cells are largely dependent upon the formation and dynamics of leader cells, and the transduction of guidance cues to the ensuing followers.

Collective cell migration plays a central role in guiding keratinocyte migration during reepithelialization, an essential component underlying the repair of wounded skin, wherein the cutaneous epidermal barrier is reinstated (***Kirfel and Herzog*** (***2004***)). Recent work from our group identified the mechanically activated ion channel, PIEZO1, as a key regulator of the reepithelialization process (***Holt et al.*** (***2021***)). Wounds generated in skin-specific *Piezo1* knockout mice (*Krt14*^{Cre};*Piezo1*$^{fl/fl}$; hereafter *Piezo1*-cKO) were found to close faster than those in littermate Control (Control$_{cKO}$) mice. On the other hand, *Krt14*^{Cre};*Piezo1*$^{cx/+}$ mice (hereafter *Piezo1*-GoF) which express a skin-specific *Piezo1* gain-of-function mutation exhibited slower wound closure relative to littermate Control (Control$_{GoF}$) mice (***Figure 1A***; ***Holt et al.*** (***2021***)). Scratch wound assays performed in monolayers of keratinocytes isolated from these mice recapitulate the *in vivo* results, confirming that PIEZO1 activity inhibits keratinocyte reepithelialization (***Figure 1B***; ***Holt et al.*** (***2021***)). Moreover, treatment of monolayers with Yoda1, a chemical agonist of PIEZO1, also resulted in delayed wound closure further indicating the channel's involvement in regulating wound closure (***Figure 1B***) (***Lacroix et al.*** (***2018***); ***Syeda et al.*** (***2015***)). Through a combined series of *in vitro* experimentation and bioimage analyses we determined that PIEZO1 channel activity increases cell retraction along the wound edge during *in vitro* wound closure assays, inhibiting advancement of cells and thus slowing wound closure. Our finding that PIEZO1 enhances retraction provided a working mechanism for how PIEZO1 activation slows wound closure, while the absence of the channel accelerates wound closure.

Interestingly, several experimental studies have highlighted that mechanical cues play a role in leader cell formation (***Dean et al.*** (***2019***); ***Vishwakarma et al.*** (***2018***)), guiding directionality (***Cai et al.*** (***2014***); ***Li et al.*** (***2012***)), and in governing the length scale of correlated motion during collective migration (***Das et al.*** (***2015***)). However, the molecular machinery underlying the mechanical regulation of collective migration are still being elucidated. Given PIEZO1's contribution to keratinocyte reepithelialization we asked whether PIEZO1 may affect the mechanoregulation of leader cells and cellular coordination during collective migration. Here, we take a combined theoretical and experimental approach to probe PIEZO1's contribution to the biophysical mechanisms underlying keratinocyte collective migration.

Mathematical modeling has emerged as a powerful technique to probe how the central components of collective migration affect migration efficiency (***Banerjee and Cristina*** (***2019***); ***Buttenschön and Edelstein-Keshet*** (***2020***); ***Thompson et al.*** (***2012***)). Since specific cell migration features are well-isolated in a mathematical model, numerical simulations provide an efficient approach to systematically investigate how biological factors contribute to the complex orchestration of collective migration. Thus, by integrating experimental data at the single cell and monolayer scales we develop and calibrate a two-dimensional multiscale model of reepithelialization. Numerical simulations using the calibrated model show that cell directionality, or the uniformity of migration direction among cells, plays a key role in recapitulating PIEZO1's effect on wound closure. Guided by our model prediction, we experimentally validate our model predictions, and identify that PIEZO1 activity reduces the distance over which cells can correlate their movements. We find that PIEZO1 activity suppresses the formation of leader cells and propose that this hinders the coordinated migration of cell subpopulations, contributing to the inhibition of collective migration during keratinocyte reepithelialization.

Results

PIEZO1 activity inhibits wound edge dynamics and leader cell formation

Efficient collective migration is driven by the formation of leader cells (***Bianco et al.*** (***2007***); ***Haeger et al.*** (***2015***); ***Reffay et al.*** (***2014***)). In light of our previous finding that PIEZO1 activity inhibits wound closure (***Holt et al.*** (***2021***)), we sought to further characterize the effect of PIEZO1 on collective migration by investigating how PIEZO1 activity may affect leader cell formation. Since the emergence of leader cells drives collective migration and increased PIEZO1 activity results in delayed wound closure, we hypothesized that the number of leader cells would be affected by PIEZO1 activity levels. We generated scratch wounds in *Piezo1*-cKO, *Piezo1*-GoF, Yoda1-treated keratinocyte monolayers and their respective controls and utilized differential interference contrast (DIC) time-lapse imaging to examine the evolution of the wound margin (***Figure 1C-E***). During reepithelialization, multicellular finger-like protrusions often form along the wound margin as cells work together to close the wound area (***Yang and Levine*** (***2020***)). At the front of these fingering structures, leader cells can be identified by their larger size and prominent lamellipodia (***Figure 1F***, ***Figure 1—figure Supplement 1***) (***Poujade et al.*** (***2007***); ***Reffay et al.*** (***2014***)). Leader cells were manually identified in time lapse images of wound closure (***Riahi et al.*** (***2015***)). As hypothesized, we found that in *Piezo1*-cKO monolayers, the monolayer edge is more featured with an increase in the number of leader cell protrusions compared to those from Control$_{cKO}$ keratinocyte monolayers (***Figure 1C, G***, ***Figure 1—figure Supplement 1A***). On the other hand in both *Piezo1*-GoF and Yoda1-treated monolayer conditions, where PIEZO1 activity is increased, the wound edge remains relatively flat throughout the imaging period indicating a decrease in the formation of leader cell protrusions compared to respective control monolayers (***Figure 1D, E, G***, ***Figure 1—figure Supplement 1B, C***). Furthermore, we noticed in *Piezo1*-cKO monolayers, that leader cells appeared to recruit more follower cells as seen

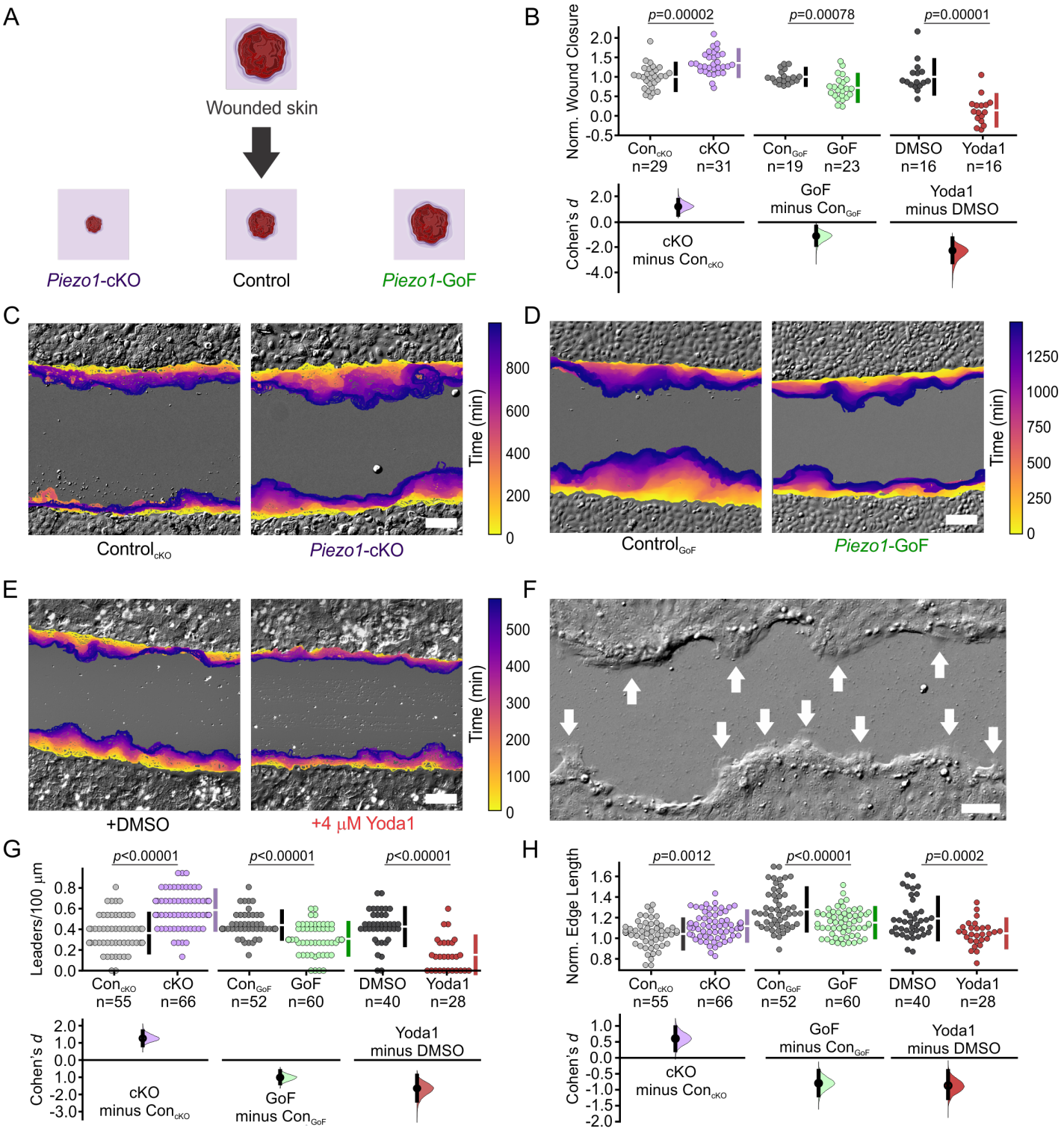

Figure 1. PIEZO1 activity inhibits wound edge dynamics and leader cell formation. **(A)** Summary schematic depicting PIEZO1's effect on keratinocyte reepithelialization reported in Holt *et al.* 2021. **(B)** Reproduced from Fig 1L in ref. (***Holt et al.*** (***2021***)) under a Creative Commons Attribution license, Cumming plot illustrating wound closure during *in vitro* scratch assays utilizing keratinocytes isolated from: $Control_{cKO}$ and *Piezo1*-cKO mice (*left*; *p* value calculated via two-sample t-test; Cohen's *d* = 1.188; images from three independent experiments), $Control_{GoF}$ and *Piezo1*-GoF mice (*middle*; *p* value calculated via two-sample t-test; Cohen's *d* = -1.128; images from four independent experiments), and DMSO-treated and 4 μM Yoda1-treated keratinocytes (*right*; *p* value calculated via Mann-Whitney test; Cohen's *d* = -2.278; images from three independent experiments). *n* in B denotes the number of unique fields of view imaged. **(C)** Representative overlay of the leading edge detected

Figure 1 continued on next page

Figure 1 continued
and segmented from DIC time-lapse images taken during *in vitro* scratch assay experiments in $\text{Control}_{\text{cKO}}$ (left) and *Piezo1*-cKO (right) monolayers. Color of the cell boundary outline indicates passage of time. Scale bar = 100 μm. The data in C are representative of three independent experiments. **(D)** Similar to C but for scratch assay experiments performed in $\text{Control}_{\text{GoF}}$ (*left*) and *Piezo1*-GoF (*right*) monolayers. The data in D are representative of four independent experiments. **(E)** Similar to C but for scratch assay experiments performed in DMSO-treated (*left*) and 4 μM Yoda1-treated (*right*) monolayers. The data in E are representative of three independent experiments. **(F)** Representative DIC image of wound closure during an *in vitro* scratch assay showing the appearance of finger-like protrusions led by leader cells (shown by white arrows). Scale bar = 100 μm. See also ***Figure 1—figure Supplement 1***. **(G)** Cumming plot showing the number of leader cells per 100 μm which were manually identified from DIC time-lapse images along the wound margin in monolayers of: $\text{Control}_{\text{cKO}}$ vs. *Piezo1*-cKO keratinocytes (*left*; *p* value calculated via two-sided permutation t-test; Cohen's *d* = 1.264), $\text{Control}_{\text{GoF}}$ vs. *Piezo1*-GoF keratinocytes (*middle*; *p* value calculated via Mann Whitney test; Cohen's *d* = -1.013), DMSO-treated vs. 4 μM Yoda1-treated keratinocytes (*right*; *p* value calculated via Mann Whitney test; Cohen's *d* = -1.647). **(H)** Cumming plot showing quantification of the normalized edge length in monolayers of: $\text{Control}_{\text{cKO}}$ vs. *Piezo1*-cKO keratinocytes (*left*; *p* value calculated via two-sided permutation t-test; Cohen's *d*= 0.598), $\text{Control}_{\text{GoF}}$ vs. *Piezo1*-GoF keratinocytes (*middle*; *p* value calculated via two-sided permutation t-test; Cohen's *d*= -0.799), DMSO-treated vs. 4 μM Yoda1-treated keratinocytes (*left*; *p* value calculated via two-sided permutation t-test; Cohen's *d*= -0.873). To account for differences in the starting edge length which might occur when scratching monolayers in H, data are normalized by dividing the scratch length at either the end of the imaging period, or at the moment the wound edges touch, by the starting scratch length. A higher normalized edge length indicates a more featured wound edge, corresponding to the presence of more leader cells. *n* in G & H denotes the number of monolayer sheets imaged. See also ***Table 1***.

Figure 1—figure supplement 1. PIEZO1 inhibits leader cell formation at wound margins.

by an increase in the width of fingering protrusions relative to $\text{Control}_{\text{cKO}}$ monolayers (***Figure 1C***, ***Figure 1—figure Supplement 1***).

To quantify the effect that PIEZO1 activity has on wound edge dynamics and leader cell protrusions, we also measured the change in the length of the wound edge within a field of view over the course of the imaging period, similar to methods employed by other groups (***Lee et al.*** (***2021***)). Any protrusions of leader cells into the wound margin would increase the length of the wound edge. Therefore a shorter wound edge would indicate less protrusions while a longer wound edge would indicate an increase in protrusions along the wound margin. We found that *Piezo1*-cKO monolayers have a longer wound edge length relative to $\text{Control}_{\text{cKO}}$ monolayers, which further supports our observation that the absence of PIEZO1 results in increased leader cells along the wound edge (***Figure 1H left***). Conversely, in both *Piezo1*-GoF and Yoda1-treated monolayers we found that edge lengths are significantly shorter than the respective control monolayers (***Figure 1H middle, right***). Thus, we find that PIEZO1 inhibits the formation of leader cells, resulting in a shorter and flatter wound edge, while the absence of the channel results in a longer and more featured wound edge due to an increase in leader cell protrusions.

Modeling PIEZO1's influence on keratinocyte collective dynamics

Due to the many intricacies underlying the biological phenomena of collective cell migration, we adopted a theoretical approach as a framework for characterizing the biophysical relationship between PIEZO1 activity, leader cell initiation and wound closure. We designed a mathematical model of keratinocyte reepithelialization in order to study how PIEZO1 activity influences this process. We first separated reepithelialization into essential phenomenological components which could be incorporated into the design of the model as manipulable variables. As such we accounted for cell motility, and cellular retraction, a process central to the migration process and one which we previously found PIEZO1 activity promoted (***Holt et al.*** (***2021***)). We incorporated into our model design: (1) the average duration of retraction events at the monolayer edge, (2) the interval between sequential edge retractions, and (3) the strength of retraction. We also incorporated two hallmarks of collective cell migration: cell-cell adhesion and the coordination of keratinocyte migration direction, or directionality, both of which have been central to mathematical models proposed by other groups (***Khain et al.*** (***2011***); ***Thompson et al.*** (***2012***); ***Holmes et al.*** (***2017***); ***Ko and Lobo*** (***2019***)). We manipulate these biological components of wound closure within our model and compare simulation results to experimental data garnered from scratch assays of PIEZO1 mutant keratinocytes.

Due to the inherent multivariate nature of our system, we utilized a partial differential equation (PDE) model to spatiotemporally describe PIEZO1's effect on reepithelialization. The PDE governing collective cell migration, which describes behavior at the monolayer scale, is derived by upscaling a discrete model at the single cell level. Simulations of wound closure, obtained by solving the nonlinear PDE numerically, enables a deeper understanding of how each model parameter contributes at both the single cell and monolayer levels. Furthermore, integration of experimental data at the single cell and monolayer scales allows for calibration of the model. We present a dimensionless version of the model here: the cell density is scaled by its maximal value, and the length and time scales are nondimensionalized using characteristic length and time scales that are described in Appendix 1 section 6.

The two-dimensional spatial discretization of a field of view containing a monolayer covered by a uniform grid of size h allows

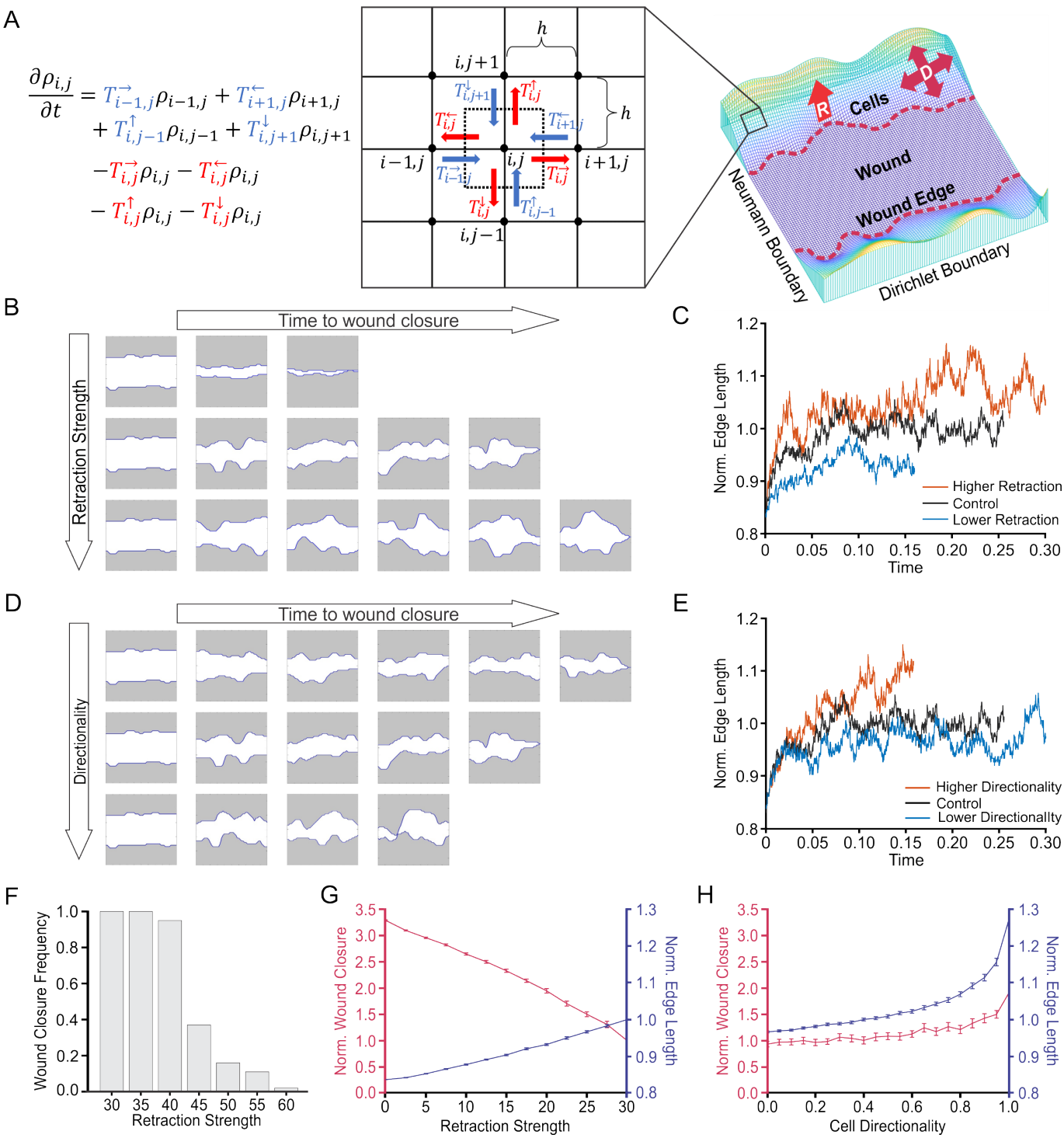

Figure 2. Cell directionality is the key model parameter which replicates PIEZO1 reepithelialization phenotypes. (A) Schematic showing a simplified visual of multiscale modeling and visualization of the simulation domain. In the semi-discrete master equation (*left*; Eq. 1), transitional probabilities associated with cell influx are highlighted in blue, while cell outflux related transitional probabilities are in red. Corresponding arrows depict this process on the grid (*middle*), indicating that the net flux is equal to the change in cell density over time at grid point (i, j). $\boldsymbol{D}$ represents directionality, and $\boldsymbol{R}$ represents retraction. **(B)** Simulation snapshots taken at equidistant time intervals depicting the evolution of the wound edge until wound closure (the moment interfaces touched) under low (*top*), Control (*middle*) and increased (*bottom*) levels of retraction strength. Shaded areas represent cell monolayers, while unshaded areas denote the cell-free space. **(C)** Plots showing quantification of the normalized edge length of simulated wounds, a measurement indicative of the number of leader cells, under different levels of retraction strength as a function of time. Shorter lines indicate simulation ending earlier due to faster wound closure. **(D, E)** Same as for (B) and (C), but

Figure 2 continued on next page

Figure 2 continued
under different levels of directionality. **(F)** The proportion of wound closure cases under different retraction magnitudes. The proportion of open wound closure cases start to decline after increasing retraction strength to 40, and almost no closure cases as approaching 60. See also ***Figure 2—figure Supplement 1***. **(G)** Line graphs showing the mean of 100 simulation results depicting the effect of retraction strength on normalized wound closure (*red; left axes*) and normalized edge length (*blue; right axes*). Error bars depict the standard error of mean. **(H)** Similar to (G) but for cell directionality. In C, E, F-H, all numbers have no unit because the model is dimensionless. See also ***Figure 2—figure Supplement 2***, and ***Table 1***.

Figure 2—figure supplement 1. Wounds fail to reach closure if parameter values exceed reasonable ranges.

Figure 2—figure supplement 2. Cell Directionality is the only parameter which replicates all experimental results.

---

the labeling of indices (i, j) in space as $\mathbf{x} = \mathbf{x}_{i,j} = (ih, jh)$, and cell density, $\rho = \rho(\mathbf{x}, t) = \rho(x, y, t)$, a function of space, $\mathbf{x} = (x, y)^T$, and time, t, can be represented by $\rho_{i,j} = \rho(\mathbf{x}_{i,j}, t)$ at time t (***Figure 2A***). The dimensionless experimental field of view is a unit square domain: $[0, 1] \times [0, 1] \in \mathbb{R}^2$ (see Appendix 1 section 6 for the details of nondimensionalization). By incorporating the essential biological components of reepithelialization (***Table 1***, bottom), we construct the following discrete master equation (***Figure 2A left***; Eq. 1), which demonstrates the change rate of cell density over time (Eq. 1; left hand side) in response to the net flux of cells (Eq. 1; right hand side):

$$\begin{aligned}\frac{\partial \rho_{i,j}}{\partial t} =& T^{\rightarrow}_{i-1,j}\rho_{i-1,j} + T^{\leftarrow}_{i+1,j}\rho_{i+1,j} + T^{\uparrow}_{i,j-1}\rho_{i,j-1} + T^{\downarrow}_{i,j+1}\rho_{i,j+1} \\ &- (T^{\rightarrow}_{i,j} + T^{\leftarrow}_{i,j} + T^{\uparrow}_{i,j} + T^{\downarrow}_{i,j}) \cdot \rho_{i,j}.\end{aligned} \tag{1}$$

Here, the T's are transitional probabilities per unit time for a given direction of movement (i.e., $T^{\rightarrow}_{i,j}$, $T^{\leftarrow}_{i,j}$, $T^{\uparrow}_{i,j}$ and $T^{\downarrow}_{i,j}$) for cells migrating between adjacent grid points (e.g., from $\mathbf{x}_{i,j}$ to $\mathbf{x}_{i+1,j}$ for $T^{\rightarrow}_{i,j}$). Each transitional probability accounts for cell motility, cell-cell adhesion, cell directionality and volume filling limitations. One component scales as $\mathcal{O}(1/h^2)$, which results in a diffusion flux that depends on the gradient of cell density. The other component scales as $\mathcal{O}(1/h)$, which results in an advection velocity independent of the cell density that mimics the influence of retraction events (see *multi-scale modeling* section in Methods, Eq. 12, 13). The continuum limit can be obtained by taking $h \to 0$:

$$\frac{\partial \rho}{\partial t} = \nabla \cdot (\boldsymbol{D}\nabla\rho + \boldsymbol{R}\rho) \tag{2}$$

which is a diffusion-advection equation where diffusion, $\boldsymbol{D}$, models cellular locomotion and directionality, whereas the advection velocity, $\boldsymbol{R}$, models retraction of the leading edge. The diffusion coefficient, or diffusivity, $\boldsymbol{D}$, is a 2×2 positive definite matrix given by:

$$\boldsymbol{D} = d \cdot (w_I \boldsymbol{I} + w_A \boldsymbol{A}) \cdot \hat{D}_\alpha(\rho), \tag{3}$$

where $d > 0$ models cell motility during collective migration. The diffusion decomposition $w_I \boldsymbol{I} + w_A \boldsymbol{A}$ combines the diffusion isotropy, where the identity matrix $\boldsymbol{I} = \boldsymbol{I}_2$ models the randomness of cellular migration, and diffusion anisotropy, where the matrix $\boldsymbol{A}$ models directed cellular migration. During wound closure, directional cues received from leader cells promote the migration of followers into the cell-free space to close the wound, thus promoting cells to have a higher probability of moving into the wound area and resulting in an anisotropic direction of diffusion. This directed motion in the experimental geometry is modeled using a diagonal matrix $\boldsymbol{A} = diag(0, 1)$ (see the *multi-scale modeling* section in Methods for the detailed derivation of this matrix decomposition). Under the convex weighting relation $w_I + w_A = 1$, the isotropic strength, $w_I \in [0, 1]$, and the anisotropic strength, $w_A \in [0, 1]$, combine matrices $\boldsymbol{I}$ and $\boldsymbol{A}$ as components of the diffusivity (Eq. 3), balancing cell migration between having a random direction and moving more persistently to close the wound (***Figure 2A right***, arrows with "D"). A higher w_A indicates cells are more likely to migrate towards the direction of closure (in the y direction) rather than migrating parallel to the direction of closure (in the x direction), while a lower w_A increases random cell movement with no tendency for a specific direction. In summary, the whole anisotropy term, w_A and $\boldsymbol{A}$, together models cell directionality, where the scalar weight, w_A, models the strength of directionality and matrix $\boldsymbol{A}$ provides the direction towards wound closure. Hereafter, w_A is referred to as cell directionality.

The scalar diffusion coefficient $\hat{D}_\alpha(\rho)$ in Eq. 3 is a polynomial of cell density ρ (Eq. 16 in the *multi-scale modeling* section in Methods) derived through a multi-scale modeling process, which includes an adhesion coefficient, $\alpha \in [0, 1]$, to model the adhesion effects between adjacent cells. Volume-filling limitations to cell movement are also modeled in $\hat{D}_\alpha(\rho)$ to hinder cells from migrating into a cell-dense area. In order to maintain a positive diffusivity, the value of α is bounded by ~ 0.66 from above (see detailed derivation in Appendix 1 section 3).

Analogous to the derivation of diffusion, retraction, $\boldsymbol{R}$ (***Figure 2A right***), is derived from the $\mathcal{O}(1/h)$ component of the discrete transitional probability (Eq. 13) by taking the limit $h \to 0$:

$$\boldsymbol{R} = (1-\rho)(1-\alpha\rho)^3 \cdot (\Delta r^{\leftrightarrow}, \Delta r^{\updownarrow})^T \in \mathbb{R}^2 \tag{4}$$

where $1-\rho$ and $(1-\alpha\rho)^3$ model the effects of volume filling and cell-cell adhesion respectively. The retraction magnitude and directions are modeled phenomenologically in $\Delta r^{\leftrightarrow}$ and $\Delta r^{\updownarrow}$ as being localized in space and time, motivated by our previous work (***Holt et al.*** (***2021***)). In particular, we assume:

1. Retraction occurs locally along the wound edge. This means only a part of wound edge cells are involved in retraction events at each time, while the rest of cells on the edge and cells within the monolayer away from the edge just migrate by diffusion.
2. Retraction occurs intermittently in time. This means no retraction event is endless, i.e., no regions retract indefinitely. Hence at a wound edge point, there is a finite interval of duration time for each retraction event, and there is also a finite interval of time between two consecutive retraction events.

Following assumptions 1 and 2 listed above, $\Delta r^{\leftrightarrow}$ and $\Delta r^{\updownarrow}$ are built as random functions of time and space, which model random retraction events near the wound edge with mean strength μ_s. A single retraction event is sustained for a random duration with mean μ_r, and any subsequent retraction will only start after a random idle duration with mean μ_{nr} (See section *retraction localization* in Methods for details). In the retraction region, cell movement is governed by a diffusion-advection equation where $\Delta r^{\leftrightarrow} = \Delta r^{\updownarrow} \approx \mu_s$ is the advection velocity in the absence of volume filling and cell-cell adhesion effects. On the other hand, retractions are negated by $\Delta r^{\leftrightarrow} = \Delta r^{\updownarrow} = 0$ in the areas of the monolayer away from the retraction region so that cells located in these regions migrate by diffusion without advection.

Since we only model the observation domain in the experiment, i.e., the region close to the wound edges as opposed to the whole experimental domain, we impose the following conditions at the domain boundaries:

$$\begin{gathered} \rho(x,0,t) = g_0(x,t), \quad \rho(x,1,t) = g_1(x,t), \\ \frac{\partial \rho(0,y,t)}{\partial x} = \frac{\partial \rho(1,y,t)}{\partial x} = 0. \end{gathered} \tag{5}$$

Horizontally on the top and bottom of the domain, the time-dependent Dirichlet boundary conditions at $\mathbf{x} = (x,0)$ and $\mathbf{x} = (x,1)$ assign cell densities to the boundary points by functions g_0 and g_1, which mimic the effect of cells that flow into the observation domain area from the monolayer roughly perpendicular to the wound edge. The functions g_0 and g_1 are random functions of space and time (See Appendix 1 Section 1 for the definitions of g_0 and g_1). Whilst vertically on the left and right sides of the domain, no-flux (Neumann) boundary conditions are used to approximate a net balance of cell influx and efflux into the observation domain roughly parallel to the wound edge, as suggested by the experiments.

The initial condition is generated by solving the PDE without retraction events for a short time period, which produces a banded heterogeneous monolayer with a cell-free region in the middle mimicking the initial wound (see Appendix 1 Section 2 for details).

Summarizing, the model depends on the following biological parameters: (1) the mean retraction duration, μ_r, (2) the mean inter-retraction duration, μ_{nr}, (3) the mean retraction strength, μ_s, (4) cell motility, d, in the absence of retraction (pure diffusion context), (5) cell-cell adhesion, α, and (6) the strength of cell directionality, w_A. Since the governing equation (Eq. 2) is a nonlinear stochastic PDE, we perform simulations by using a finite difference method to solve the PDE numerically for cell density $\rho(\mathbf{x},t)$ on the simulation domain over time until wound closure. Multiple simulations are performed under each condition to quantify the variability for the subsequent data analysis (See Method section *numerical scheme* for detail), from which we investigate how each model parameter influences collective migration during reepithelialization.

Cell directionality is the key model parameter which replicates PIEZO1 reepithelialization phenotypes

Simulations of wound closure provide insight into how individual model parameters affect the wound closure process (***Figure 2B-E***). Thus, through a parameter study, we can explore the effects of model parameters on two experimentally-measured phenotypes affected by PIEZO1 activity during keratinocyte reepithelialization: (1) the rate of normalized wound closure and (2) normalized wound edge length, a measurement which we see is correlated with leader cell presence (***Figure 1G, H***). During simulations we found that wounds would fail to close if parameters exceed a reasonable range (***Figure 2F***, ***Figure 2—figure Supplement 1***). For instance, when retraction strength is set too high, cells are unable to overcome retractions of the wound edge which causes wounds to remain

experimental observations	norm. wound closure	norm. edge length
Piezo1-cKO relative to $\text{Control}_{\text{cKO}}$	+	+
Piezo1-GoF relative to $\text{Control}_{\text{GoF}}$	−	−
Yoda1-treated relative to DMSO-treated	−	−

model parameter	norm. wound closure	norm. edge length
retraction strength	−	+
retraction duration	−	+
inter-retraction duration	+	−
cell motility	+	−
cell-cell adhesion	−	+
cell directionality	**+**	**+**

Table 1. Cell directionality is the key model parameter which replicates PIEZO1 reepithelialization phenotypes: *Top*: Summary table of monolayer experimental results on normalized wound closure and wound edge length. See also ***Figure 1***. *Bottom*: Summary table of simulation results, depicting the effect of model parameters on normalized wound closure and wound edge length. For model parameters, single cell parameters (retraction strength, retraction duration, inter-retraction duration and cell motility) are separated from parameters which come from collective cell settings (cell-cell adhesion and cell directionality). A "+" indicates the wound feature is positively correlated with the model parameter, e.g., wound edge length increases with increased retraction strength, whereas "−" indicates a negative correlation, e.g., normalized wound closure is reduced with increasing retraction strength. Bolded italicized text denotes model parameters which correspond with experimental trends. See also ***Figure 2G, H*** and ***Figure 2—figure Supplement 2***.

open indefinitely (***Figure 2F***). This model prediction is consistent with experimental results where Yoda1 treatment sometimes resulted in an increase in wound area during wound closure assays (***Figure 1B***) (***Holt et al.*** (***2021***)).

By plotting the average rate of wound closure and edge length across multiple simulations we can see how the setting of individual model parameters compares to experimental trends we observe (***Figure 2G, H***; ***Figure 2—figure Supplement 2***). We find that increasing the retraction strength parameter hinders wound closure, a result which is in line with the mechanism proposed in Holt *et al.* 2021 (***Holt et al.*** (***2021***)) (***Figure 2G***). However, our parameter study also shows that increased retraction strength results in a longer wound edge length, suggesting an increase in leader cell-like protrusions along the simulated wound margin. This contradicts our experimental observations in which a shorter wound edge length with less leader cells accompanies delayed wound closure (***Figure 2G***; ***Table 1***). Similarly, we find that lower retraction strength elicited faster wound closure with shorter edge lengths due to less leader cell-like protrusions which also contradicts our experimental results (***Figure 2G***). Together, these results indicate that there is more to PIEZO1's role in cell migration than retraction alone.

To identify possible contributors of wound closure regulation influenced by PIEZO1 activity, we performed an extensive parameter study in which we made adjustments to the model parameters of: cell-cell adhesion, retraction duration, inter-retraction duration, cell motility and directionality. We found that manipulation of all parameters aside from directionality fail to replicate the observed experimental results, i.e., faster wound closure accompanying a longer edge length, or conversely, delayed closure occurring with a shorter edge length (***Table 1***; ***Figure 2—figure Supplement 2***). By increasing the directionality parameter within our model, wounds close faster with longer edge lengths due to the presence of more leader cell-like protrusions, replicating experimental observations in *Piezo1*-cKO monolayers (***Figure 2H***). On the other hand, under low directionality parameter conditions cells migrate more aimlessly, with formation of fewer leader-cell like protrusions along the wound edge and with inhibited closure, similar to observations from *Piezo1*-GoF and Yoda1-treated wounds (***Figure 2H***). Taken together, our parameter study predicts that while other model parameters, including retraction strength, affect keratinocyte migration, cell directionality plays a key role in modeling PIEZO1 inhibition of keratinocyte reepithelialization.

PIEZO1 activity is predicted to regulate wound closure by hindering cell directionality

Our modeling parameter study reveals how altering individual model parameters one at a time affects wound closure through numerical simulations. However, experimental results reveal that PIEZO1 activity may alter more than one model parameter, which may generate compensating effects that reduce the contribution of cell directionality in the experimental setting. Therefore, we sought to further constrain the mathematical model by incorporating model parameters derived from experimental data. To this end, we utilized and expanded upon analyses performed on single migrating keratinocytes in our previous study (***Holt et al.*** (***2021***)), to compile an experimental dataset characterizing PIEZO1's effect on: cell motility, retraction duration, inter-retraction duration and cell retraction strength (***Figure 3A***, ***Table 2***; ***Figure 3—figure Supplement 1***). Cell motility parameters were calculated by extracting

experimental observations	retraction duration	inter-retraction duration	retraction strength	cell motility
Piezo1-cKO relative to $\text{Control}_{\text{cKO}}$	+	+	+	+
Piezo1-GoF relative to $\text{Control}_{\text{GoF}}$	+	−	+	∼
Yoda1-treated relative to DMSO-treated	−	−	+	∼

Table 2. PIEZO1 activity affects single cell migration: Summary table of single cell migration dataset features initially captured and measured quantitatively during single cell experiments (i.e., kymograph, cell protrusion analyses, single cell tracking assays). A "+" indicates an increase, "−" indicates a decrease, and "∼" indicates no statistically significant change between Control and Test condition. All data aside from DMSO and Yoda1 cell motility (***Figure 3—figure Supplement 2***) was initially published in (***Holt et al.*** (***2021***)). Actual data values for each condition can be found listed in ***Figure 3—figure Supplement 1***.

cell speed information from single cell tracking experiments which were previously performed using single *Piezo1*-cKO and *Piezo1*-GoF keratinocytes (***Holt et al.*** (***2021***)) (***Figure 3A left***; ***Table 1***; ***Figure 3—figure Supplement 1***). We expanded upon this work by also tracking individually migrating Yoda1 and DMSO-treated keratinocytes to incorporate the effect of Yoda1 on cell motility into our model predictions. Similar to our observations in *Piezo1*-GoF keratinocytes, Yoda1 treatment had no effect on the motility of single migrating keratinocytes compared to DMSO-treated control cells (***Figure 3—figure Supplement 2***). To find the average duration of retractions and intervals between successive retractions for all experimental conditions (*Piezo1*-cKO, *Piezo1*-GoF, Yoda1 and the respective controls), we utilized two analysis methods performed in our previous study (***Holt et al.*** (***2021***)): (1) kymographs (***Figure 3A right***), which graphically depict the retraction and inter-retraction durations of the leading edge of migrating keratinocytes, and (2) a cell protrusion quantification software, ADAPT (***Barry et al.*** (***2015***)), which quantifies the strength of retraction events at the leading edge. Thus, from these measurements (***Figure 3A***, ***Table 2***, ***Figure 3—figure Supplement 1***), we can calibrate our model parameters based on experimental measurements, enabling us to make experimentally relevant predictions regarding PIEZO1's influence on wound closure behavior.

To calibrate our model, we created a respective simulation control for each experimental condition (*Piezo1*-cKO, *Piezo1*-GoF and Yoda1-treated) by fixing the values of model parameters to a basecase, where the frequency of retraction was set to be the same as the corresponding experimental control. For a given experimental condition, the model parameters related to retraction (retraction duration, inter-retraction duration, retraction strength) and cell motility were adjusted from the control condition by the same proportions as their experimentally-measured changes relative to the control condition (***Figure 3A***, ***Table 2***; ***Figure 3—figure Supplement 1***). In particular, the mean retraction and inter-retraction durations μ_r and μ_{nr}, the cell motility d and the mean retraction strength μ_s are changed proportionally in the model (see Method section *model parameter adjustment* for details). With cell-cell adhesion and cell directionality unchanged compared to control, we find that while we can replicate simulated monolayers of *Piezo1*-GoF keratinocytes having slower wound closure compared to simulated $\text{Control}_{\text{GoF}}$ monolayers, we fail to observe the expected decreasing change in leader cell-like protrusions as indicated by a smaller simulated monolayer edge length (***Figure 3B***). However, by lowering the collective migration parameter of directionality, we recapitulate the experimental phenotype of both a shorter edge length and slower wound closure in simulated *Piezo1*-GoF monolayers (***Figure 3B***). On the other hand, we see that model simulations calibrated by the single cell migration dataset for both *Piezo1*-cKO and Yoda1-treated keratinocytes reproduce the expected experimental trends; however, by incorporating changes to directionality we observe a stronger effect (***Figure 3C, D***). Notably, we observe that adjustment of cell-cell adhesion parameters, another model parameter integral to collective migration, fails to replicate all experimental results, reinforcing that directionality plays a primary role in PIEZO1's effect on reepithelialization (***Table 3***; ***Figure 3—figure Supplement 3***). Taken together, these studies demonstrate that only by including alterations to directionality are we able to mimic all experimental phenotypes. Thus, our model predicts that PIEZO1 activity affects cell directionality within monolayers such that increased PIEZO1 activity inhibits cells ability to move cohesively during collective migration, ultimately delaying wound closure. On the other hand, in monolayers which lack *Piezo1* expression, cells are predicted to have clearer directionality signals and recruit more follower cells to close the wound faster.

PIEZO1 activity inhibits persistence of direction during keratinocyte collective migration

To test our model's prediction we first utilized a cell tracking assay to examine the motility of individual cells during collective migration. To track the movement of individual cells within monolayers we utilized the live-cell DNA stain SiR-Hoechst to label individual nuclei within monolayers (***Lukinavičius et al.*** (***2015***)). After imaging collective cell migration over the course of several hours, we tracked the movement of individual nuclei and analyzed the resulting cell trajectories (***Figure 4A-C***). Given the different genetic backgrounds between conditions (i.e. *Piezo1*-cKO, *Piezo1*-GoF, Yoda1-treated) and the differences observed in migration

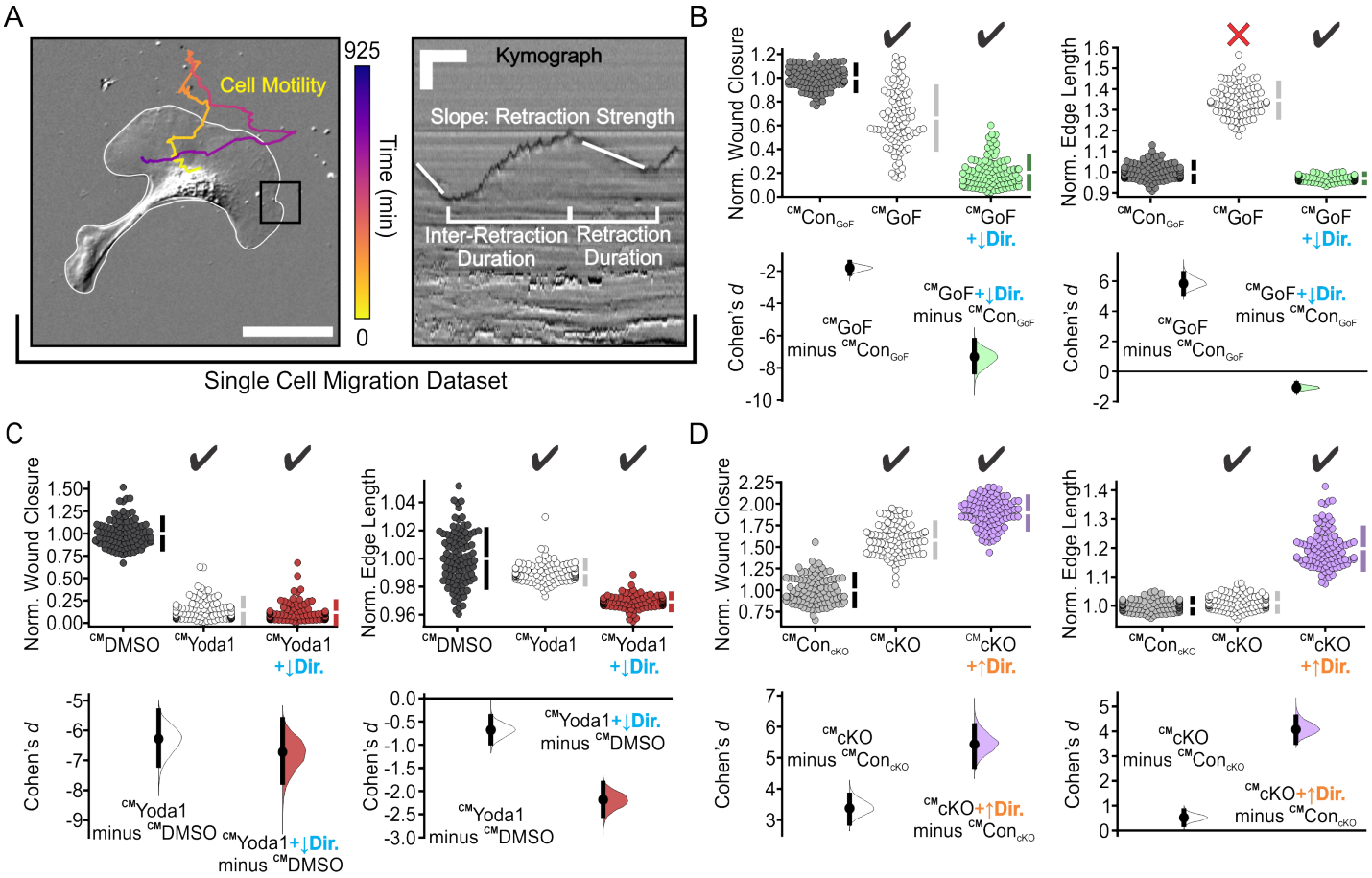

Figure 3. PIEZO1 activity is predicted to regulate wound closure by hindering cell directionality. **(A)** Schematic depicting experimentally measured features used to generate the single cell migration dataset. Left, representative still image of migrating keratinocyte with cell trajectory overlaid derived from tracking cell motility during time-lapse experiments. Color denotes passage of time such that yellow is the starting position and purple denotes track end position. Cell Boundary is in white. Scale bar = 100 μm. Kymographs (*right*) taken at the leading edge of migrating cells (e.g. similar to black box in the left image) are used to obtain information regarding inter-retraction duration and retraction duration. The cell protrusion quantification software, ADAPT was used to gain information regarding retraction strength. Scale bar = 10 μm, Time bar = 5 min. **(B)** Cumming plots showing simulation results using the calibrated model (^{CM}) to predict how PIEZO1 affects normalized wound closure (*left plots*) and wound edge length (*right plots*) in simulated Control$_{GoF}$ monolayers (*gray*), *Piezo1*-GoF monolayers without altered directionality parameters (*white*), and *Piezo1*-GoF monolayers with cell directionality decreased (*blue)*. See Method section *model parameter adjustment* for the details. **(C)** Similar to B but using simulation results from DMSO-treated monolayers (*gray*), Yoda1-treated monolayers without altered directionality parameters (*white*), and Yoda1-treated monolayers with directionality decreased (*blue)*. **(D)** Similar to B but using simulation results from Control$_{cKO}$ monolayers (*gray*), *Piezo1*-cKO monolayers without altered directionality parameters (*white*), and *Piezo1*-cKO monolayers with directionality increased (*orange)*. In B-D, n = 100 simulation results for each condition, and ^{CM} denotes "Calibrated Model". To account for differences between control cases, data are normalized by rescaling to the mean of the corresponding control. Larger normalized wound closure indicates faster wound closure, while a smaller normalized wound closure indicates slower wound closure. Similarly, a larger normalized edge length indicates a more featured wound while a smaller normalized edge length indicates a flatter or less featured wound. Black check marks at the top of each plot condition indicate that simulation results match experimental trends while a red cross indicates simulation fails to match the experiment trends. See also ***Table 3***. For comparison with experimental data see ***Figure 1B, G, H***.

Figure 3—figure supplement 1. PIEZO1 activity affects single cell migration.

Figure 3—figure supplement 2. Yoda1 has no effect on single cell migration.

Figure 3—figure supplement 3. Varying cell-cell adhesion fails to match all the experimental trends.

model parameter sets	norm. wound closure	norm. edge length	experimental match
^{CM}Control$_{GoF}$ to ^{CM}GoF	–	+	✗
^{CM}Control$_{GoF}$ to ^{CM}GoF + adhesion ↑	––	++	✗
^{CM}Control$_{GoF}$ to ^{CM}GoF + adhesion ↓	+	–	✗
^{CM}Control$_{GoF}$ to ^{CM}GoF + directionality ↓	––	–	✓
^{CM}DMSO to ^{CM}Yoda1	–	–	✓
^{CM}DMSO to ^{CM}Yoda1 + adhesion ↑	––	+	✗
^{CM}DMSO to ^{CM}Yoda1 + adhesion ↓	+	––	✗
^{CM}DMSO to ^{CM}Yoda1 + directionality ↓	––	––	✓
^{CM}Control$_{cKO}$ to ^{CM}cKO	+	+	✓
^{CM}Control$_{cKO}$ to ^{CM}cKO + adhesion ↑	–	++	✗
^{CM}Control$_{cKO}$ to ^{CM}cKO + adhesion ↓	++	–	✗
^{CM}Control$_{cKO}$ to ^{CM}cKO + directionality ↑	++	++	✓

Table 3. Directionality recovers monolayer closure behavior from single cell data: Summary table depicting simulation results using the calibrated model (^{CM}) to predict how PIEZO1 affects normalized wound closure and normalized edge length with altered adhesion and directionality parameters. A "+" indicates a parameter set has a predicted increase upon an experimental measure while a "–" indicates a predicted decrease. Double signs (++/––) represent a stronger observed effect on the simulated measure than single signs (+/–). Red font and cross mark ✗ indicate that model predictions calibrated by the "Single Cell Migration" dataset do not match experimental trends (***Table 1***), while a check mark ✓indicates that model predictions are consistent with experimental results. See also ***Figure 3*** and ***Figure 3—figure Supplement 3***.

properties for these different backgrounds (***Holt et al.*** (***2021***)), keratinocytes are only compared to control conditions of the same genetic background for all analyses. The mean squared displacement (MSD) is a common metric for analyzing cell displacement as a function of time. Replicating our single cell migration observations (***Holt et al.*** (***2021***)), we observe that individual tracked nuclei within *Piezo1*-cKO monolayers have MSDs that are greater than that of Control$_{cKO}$ cells, demonstrating a larger area explored (***Figure 4D***). Measurement of the instantaneous cellular speed reveals that, similar to our previous observations, *Piezo1*-cKO cells migrate faster relative to littermate Control$_{cKO}$ cells (***Figure 4—figure Supplement 1A***).

On the other hand, cells from both *Piezo1*-GoF and Yoda1-treated monolayers have MSDs that are significantly smaller (***Figure 4E, F***). This effect is distinct from our observation in single migrating cells, where we observed that *Piezo1*-GoF keratinocytes migrate farther than Control$_{GoF}$ cells (***Holt et al.*** (***2021***)), and that Yoda1-treatment has no difference relative to DMSO-treated control cells (***Figure 3—figure Supplement 2A***). Moreover, in both *Piezo1*-GoF and Yoda1-treated monolayers we observe that increased PIEZO1 activity inhibits migration speed (***Figure 4—figure Supplement 1B, C***). This observation also differs from our single cell migration observations in which both *Piezo1*-GoF and Yoda1-treated keratinocytes have no difference in migration speed compared to respective control cells. Our observed differences for PIEZO1's effect on speed and MSD between single cell and collective migration results may be attributed to additional mechanical information from cell-cell interactions during collective migration affecting activation of PIEZO1.

Since directionality can, in part, be inferred by how straight the trajectories of cells in a collectively migrating group are, we measured the directional persistence of individual cell trajectories. The directional persistence of a cell can be quantified by measuring the velocity autocorrelation of cell trajectories (***Gorelik and Gautreau*** (***2014***)). The randomness in direction of a cell's trajectory is indicated by how rapidly its velocity autocorrelation function decays: autocorrelation curves which decay slower indicate cells that have straighter migration trajectories. Measurement of the velocity autocorrelation shows that *Piezo1*-cKO keratinocytes migrating in cell monolayers move straighter than Control$_{cKO}$ cells (***Figure 4G***), similar to our previous findings in single migrating cells. In both *Piezo1*-GoF and Yoda1-treated keratinocytes, cells move less straight than their respective controls (***Figure 4H, I***). This finding also differs from findings in single cell migration results wherein Yoda1-treatment does not change directional persistence (***Figure 3—figure Supplement 2***) while the *Piezo1*-GoF mutation induces straighter trajectories during single cell migration (***Holt et al.*** (***2021***)).

Taken together, our results show that PIEZO1 activity inversely correlates with both cell speed and the persistence of migration direction during keratinocyte collective migration. Our observation that the directional persistence of individual keratinocytes within a monolayer is inhibited by PIEZO1 activity during collective cell migration provides initial support for our model's prediction that cell directionality is affected by PIEZO1 activity.

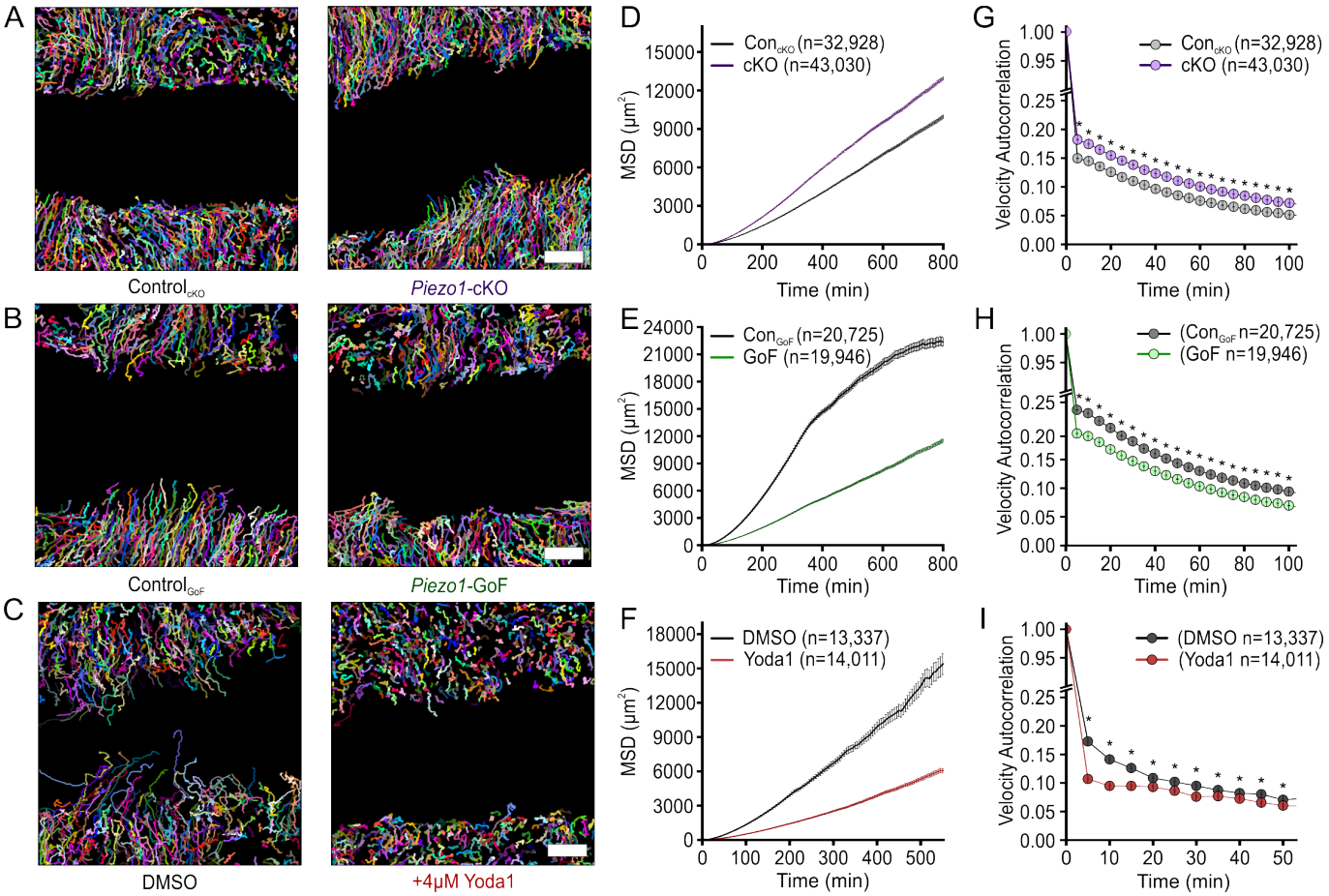

Figure 4. PIEZO1 activity inhibits persistence of direction during keratinocyte collective migration. (A-C) Representative field of view depicting individual cell trajectories derived from tracking **(A)** Control$_{cKO}$ (*left*) and *Piezo1*-cKO (*right*) keratinocytes, **(B)** Control$_{GoF}$ (*left*) and *Piezo1*-GoF (*right*) keratinocytes, and **(C)** DMSO-treated (*left*) and 4 μM Yoda1-treated (*right*) keratinocytes during collective migration experiments. Trajectory color depicts individual cell trajectories. Scale bar=100 μm. **(D-F)** Average mean squared displacement (MSD) plotted as a function of time for: **(D)** Control$_{cKO}$ (*gray*) and *Piezo1*-cKO (*purple*) keratinocytes, **(E)** Control$_{GoF}$ (*gray*) and *Piezo1*-GoF (*green*) keratinocytes, and **(F)** DMSO-treated (*gray*) and 4 μM Yoda1-treated (*red*) keratinocytes. All error bars plotted as SEM, in some instances error bars are smaller than symbols. **(G-I)** Average velocity autocorrelation measurement of: **(G)** Control$_{cKO}$ (*gray*) and *Piezo1*-cKO (*purple*) keratinocytes, **(H)** Control$_{GoF}$ (*gray*) and *Piezo1*-GoF (*green*) keratinocytes, and **(I)** DMSO-treated (*gray*) and 4 μM Yoda1-treated keratinocytes, plotted as a function of time (* denotes *p* value<0.0001 as calculated via Kolmogorov–Smirnov test). For Control$_{cKO}$ and *Piezo1*-cKO data plotted in A, D, G, images taken from three independent experiments. For Control$_{GoF}$ and *Piezo1*-GoF data plotted in B, E, H, images taken from four independent experiments. For DMSO-treated and 4 μM Yoda1-treated keratinocyte data plotted in C, F, I, images taken from three independent experiments. See also ***Figure 4—figure Supplement 1***.

Figure 4—figure supplement 1. PIEZO1 inhibits keratinocyte speed during collective cell migration.

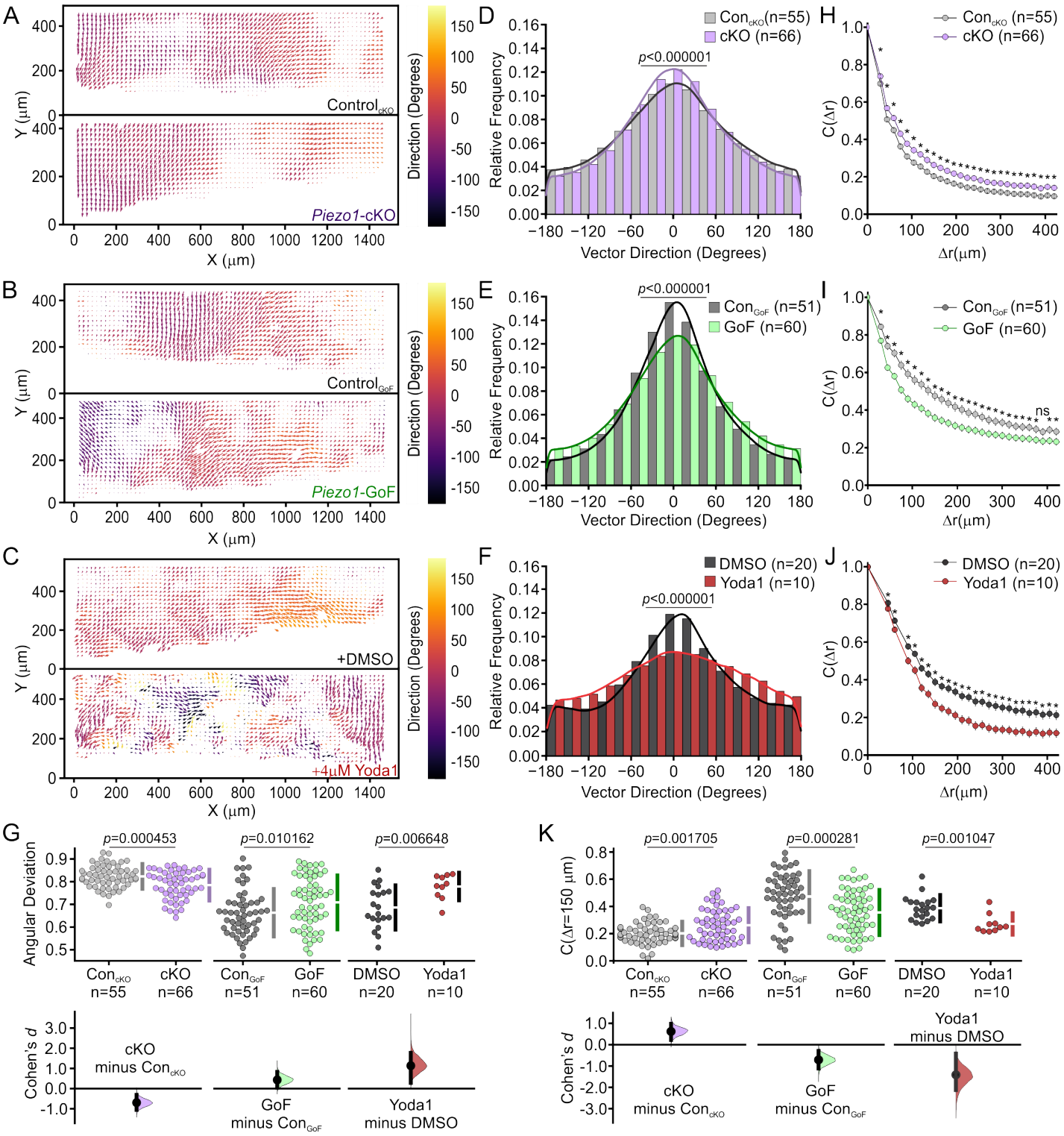

Figure 5. PIEZO1 activity inhibits the coordination of cellular motion during wound closure. (A-C) Representative mean Particle Image Velocimetry (PIV) flow fields derived from time-lapse images of labeled nuclei from collectively migrating monolayers of: **(A)** Control$_{cKO}$ (*Top*) and *Piezo1*-cKO (*Bottom*) keratinocytes, **(B)** Control$_{GoF}$ (*Top*) and *Piezo1*-GoF (*Bottom*) keratinocytes, and **(C)** DMSO-treated (*top*) and 4 μM Yoda1-treated keratinocytes (*Bottom*) during time-lapse scratch assay experiments. An individual flow field comprises either the upper or lower monolayer sheet of a scratch assay. Flow fields are oriented such that for the Y-direction, 0 μm is positioned within the cell free region. **(D-F)** Distribution plots showing the relative frequency of velocity vector direction for: **(D)** Control$_{cKO}$ (*gray*) and *Piezo1*-cKO (*purple*) monolayers, **(E)** Control$_{GoF}$ (*gray*) and *Piezo1*-GoF (*green*) monolayers, and **(F)** DMSO-treated (*gray*) and Yoda1-treated (*red*) monolayers. For D-F, *p* value calculated by Chi-squared test.

Figure 5 continued on next page

Figure 5 continued

(G) Cummings plot showing the mean angular deviation, or the variability in velocity direction isolated from PIV flow fields in: $\text{Control}_{\text{cKO}}$ vs. *Piezo1*-cKO monolayers (*left*; *p* value calculated via two-sample t-test; Cohen's *d* = -0.697), $\text{Control}_{\text{GoF}}$ vs. *Piezo1*-GoF monolayers (*middle*; *p* value calculated via two-sample t-test; Cohen's *d* = 0.43) or DMSO-treated vs. 4 μM Yoda1-treated monolayers (*right*; *p* value calculated via two-sample t-test; Cohen's *d* = 1.135). Data are normalized such that 1 indicates highly random velocity directions and 0 indicates highly uniform velocity directions. **(H-J)** Spatial autocorrelation, $C(\Delta r)$, of the radial velocity component, which is a measure of the spatial coordination of neighboring cells in monolayers, plotted as a function of increasing length scales of: **(H)** $\text{Control}_{\text{cKO}}$ (*gray*) and *Piezo1*-cKO (*purple*) keratinocytes, **(I)** $\text{Control}_{\text{GoF}}$ (*gray*) and *Piezo1*-GoF (*green*) keratinocytes, and **(J)** DMSO-treated (*gray*) and Yoda1-treated (*red*) keratinocytes. For H, I, J * denotes a statistically significant difference, and ns denotes not statistically significant as determined by one way ANOVA test. Specific *p* values for plotted points can be found in ***Figure 5—figure Supplement 2***. See also ***Figure 5—figure Supplement 1***. (**K**) Local spatial coordination, $C(\Delta r = 150\ \mu m)$, of keratinocytes where the correlation value is set at 150 μm to measure the coordination of motion with neighboring cells in: $\text{Control}_{\text{cKO}}$ vs. *Piezo1*-cKO monolayers (*left*; *p* value calculated via two-sample t-test; Cohen's *d* = 0.61969), $\text{Control}_{\text{GoF}}$ vs. *Piezo1*-GoF monolayers (*middle*; *p* value calculated via two-sample t-test; Cohen's *d* = -0.711113) or DMSO-treated vs. 4 μM Yoda1-treated monolayers (*right*; *p* value calculated via Mann-Whitney test; Cohen's *d* = -1.412). *n* in B, C, E, F, H, I, J and K denotes the number of monolayer sheets imaged. For $\text{Control}_{\text{cKO}}$ and *Piezo1*-cKO data plotted in A, D, G (*left*), H, and K (*left*), images are taken from three independent experiments. For $\text{Control}_{\text{GoF}}$ and *Piezo1*-GoF data plotted in B, E, H (*middle*), I, and K (*middle*), images are taken from four independent experiments. For DMSO-treated and 4 μM Yoda1-treated keratinocyte data plotted in C, F, H (*right*), J, and K (*right*), images are taken from two independent experiments.

Figure 5—figure supplement 1. PIEZO1 inhibits the length scale of spatial autocorrelation in keratinocytes.

Figure 5—figure supplement 2. Specific *p* values for plotted points seen in Figure 5 H-J.

PIEZO1 activity inhibits the coordination of cellular motion during wound closure

The coordinated movement of keratinocytes during wound reepithelialization depends on the large-scale interactions of multiple cells as they work together to close wounds. While tracking individual cells in a monolayer provides useful information regarding the locomotion of individual cells, it does not fully describe the dynamics of collectively migrating cells. To further validate our model's prediction that PIEZO1 activity inhibits cell directionality and to characterize the effect of PIEZO1 on large scale cellular interactions during wound closure we utilized particle image velocimetry (PIV). PIV is an optical method of flow visualization which allows us to dynamically map the velocity fields of migrating keratinocytes within a monolayer during wound closure (***Lee et al.*** (***2016***); ***Petitjean et al.*** (***2010***); ***Vedula et al.*** (***2012***)). By isolating the individual velocity vectors comprising a monolayer's vector field and mapping the frequency of vector directions for samples from different conditions (e.g. *Piezo1*-cKO, *Piezo*-GoF, and Yoda1), we can visualize how PIEZO1 affects the directionality and overall coordination of motion between cells during wound closure (***Figure 5A-C***).

Frequency distributions of velocity direction illustrate that *Piezo1*-cKO cells flow towards the wound margin (denoted by 0 degrees) to a greater extent than littermate $\text{Control}_{\text{cKO}}$ cells (***Figure 5D***). On the other hand, we find that both *Piezo1*-GoF and Yoda1-treated monolayers show a loss in directional migration as illustrated by the broader distribution of vector directions compared to vectors isolated from the respective control monolayers (***Figure 5E, F***). PIEZO1's effect on cell directionality can be further parameterized by measuring the angular deviation, or the variability in velocity direction for all vectors within a PIV vector field. Thus, the range of the angular deviation indicates how coordinated the direction of cellular motion is within an entire monolayer field of view such that a higher angular deviation indicates less coordination. We observe that *Piezo1*-cKO monolayers have a lower average angular deviation value relative to $\text{Control}_{\text{cKO}}$ monolayers, indicating a smaller spread in velocity direction (***Figure 5G left***). This is opposed to *Piezo1*-GoF and Yoda1-treated monolayers which both show a higher angular deviation than the respective controls, further signifying that PIEZO1 activity promotes less directional migration (***Figure 5G middle, right***). We note that any difference in the angular deviation between control conditions can likely be attributed to different genetic backgrounds between control conditions.

Recognizing that the synchronized movement of groups of cells during collective migration relies upon the coordination of migration direction across individual cells, we next looked at how PIEZO1 activity affects the distance over which cells align, or correlate, their motion within a monolayer. To do this, we determine how alike the movement of nearby cells is by calculating the average spatial autocorrelation of velocity vectors, ($C(\Delta r)$), which measures the degree of correlation between velocity vectors of cells at increasing length scales within a monolayer (***Figure 5H-K***). If keratinocytes within a monolayer are migrating together with high directional uniformity we expect a higher autocorrelation value, while a lower autocorrelation value indicates that individual keratinocytes are moving more independently of one another. Therefore, the decay rate of the average spatial autocorrelation curve indicates how coordinated a given cell's direction of motion is to that of another cell located at iteratively increasing distances away (***Figure 5H-J***). Measurement of the spatial autocorrelation in *Piezo1*-cKO and $\text{Control}_{\text{cKO}}$ monolayers illustrate that *Piezo1*-cKO cells show an increase in coordination with cells at greater distances relative to $\text{Control}_{\text{cKO}}$ cells, as indicated by a slower decay of the

average *Piezo1*-cKO autocorrelation curve (***Figure 5H***). The length constant, or distance at which the spatial autocorrelation reaches a value of 0.37, was estimated by fitting an exponential curve to our experimental dataset. Calculations of the length constant for *Piezo1*-cKO cells show an increase in coordination 21.471 μm farther than $\text{Control}_{\text{cKO}}$ (***Figure 5H***, ***Figure 5—figure Supplement 1***). Moreover, to quantify the coordination between nearby cells we measure the spatial autocorrelation values at 150 μm, the distance of a few cell-lengths away. Measurement of local autocorrelation values in *Piezo1*-cKO keratinocytes cells show an increased level of coordination of locomotion with neighboring cells compared to cells in $\text{Control}_{\text{cKO}}$ monolayers (***Figure 5H, K***). In contrast, both *Piezo1*-GoF and Yoda1-treated monolayers exhibit less coordinated movement with neighboring cells when compared to control cells (***Figure 5I-K***). Length constants in Yoda1 treated and *Piezo1*-GoF cells show a 58.559 μm and 85.541 μm decrease, respectively, in their coordination of motion relative to the respective control monolayers (***Figure 5I, J***, ***Figure 5—figure Supplement 1***). Therefore, we find that PIEZO1 activity disrupts the distance over which cells coordinate their motion during wound closure which inhibits the efficiency of collective migration. Taken together, our experimental findings support our model predictions that PIEZO1 inhibits cell directionality impeding coordinated migration of keratinocytes during collective migration.

Discussion

Mechanical cues have been highlighted to play a prominent role in facilitating the coordinated polarization of individual cells within a collective, regulating the speed and directionality of collective migration (***Ladoux and Mège*** (***2017***)). We recently identified the mechanically activated ion channel PIEZO1 as being a key regulator of wound healing: keratinocytes with increased PIEZO1 activity exhibited delayed wound healing while decreased PIEZO1 activity resulted in faster wound healing (***Holt et al.*** (***2021***)). Given PIEZO1's role in wound healing, we explored PIEZO1's effect on leader cell formation and directionality during collective keratinocyte migration. By taking a combined integrative multiscale modeling and experimental approach we identified that PIEZO1 activity suppresses leader cell formation, limits the directionality of cells, and reduces the distance by which keratinocytes can coordinate their directionality. Therefore, we find that PIEZO1 contributes to the molecular mechanisms that couple mechanical forces to the correlated cellular motions underlying collective migration.

In order to describe the inherent biological complexities underlying keratinocyte reepithelialization we adopted mathematical modeling as a tool to systematically investigate how aspects of collective cell migration affect wound closure. Through the development of a two-dimensional multiscale model of wound closure, we investigated how components of wound closure including cell motility, cell-cell adhesion, cell-edge retraction and the coordination of migration direction between cells, or directionality, change with manipulation of PIEZO1 activity. Through numerical simulations, we incorporated experimental data to calibrate our model and match keratinocyte monolayer behavior. We examined how model parameters impacted two attributes of wound closure which we experimentally find are affected by PIEZO1 activity: the rate of wound closure and the edge length of simulated monolayers, which served as a measure of leader cell formation. From these studies, the directionality of cells was identified as a key model parameter predicted to be impaired by PIEZO1 activity during wound closure.

Our model prediction guided the design of validation experiments and subsequent bioimage analyses, in which we confirmed the model prediction and demonstrated that PIEZO1 activity inhibits the ability of local subpopulations of cells to coordinate their movements across distances during collective migration. Altogether, we identified that PIEZO1 activity inversely correlates with the number of leader cells along the wound edge which in turn determines the directed migration of cell collectives during keratinocyte reepithelialization. Taken together with our previous work (***Holt et al.*** (***2021***)), we propose that PIEZO1-mediated retraction inhibits leader cell formation, which disrupts the uniform polarization of groups of cells and underlies the inhibition of collective migration during wound closure. This proposal is consistent with findings by other groups where pharmacologically increasing the contractile forces within monolayers was found to inhibit leader cell formation (***Dean et al.*** (***2019***); ***Riahi et al.*** (***2015***); ***Vishwakarma et al.*** (***2018***)).

During collective migration, the multicellular movement and corresponding polarization of cell clusters is dependent on signal transduction from leader cells to the ensuing follower cells (***Haeger et al.*** (***2015***); ***Hakim and Silberzan*** (***2017***); ***Ladoux and Mège*** (***2017***)). Leader cells located at the front of these collectives transmit directional cues to follower cells through intercellular mechanical forces and biochemical cues which are communicated via cell adhesion molecules such as E-cadherin (***Boocock et al.*** (***2020***); ***Cai et al.*** (***2014***); ***Hino et al.*** (***2020***); ***Khataee et al.*** (***2020***); ***Li et al.*** (***2012***); ***Oelz et al.*** (***2019***); ***Serra-Picamal et al.*** (***2012***)). Both theoretical (***Bajpai et al.*** (***2021***); ***Holmes et al.*** (***2017***)) and experimental studies (***Li and Wang*** (***2018***)) have highlighted the role that cell-cell adhesions play in determining polarization dynamics and motility in multicell systems. It is possible that PIEZO1 coordinates mechanical forces communicated at cell-cell junctions during the collective migration of keratinocytes, however further studies would be needed to elucidate this relationship. Consistent with this idea, recent work by Wang *et al.* observed that E-cadherin interacts with the PIEZO1 channel in Madin-Darby canine kidney cells (***Wang et al.*** (***2022***)).

Our previous work identified that PIEZO1 enrichment and activity induces cell retraction in single keratinocytes as well as along the wound edge of monolayers during *in vitro* scratch assays (***Holt et al.*** (***2021***)). Here we demonstrate that monolayer conditions with elevated PIEZO1 activity lack leader cell formations and display reduced coordinated movement of cells. Interestingly, retraction forces generated by follower cells have been seen to promote the formation of leader cells along the wound edge (***Vishwakarma et al.*** (***2018***)). Thus, it appears that collective migration requires carefully-regulated and coordinated levels of retraction. Consistent with this, Vishwakarma *et al.* found that pharmacologically adjusting the level of actomyosin contractility within monolayers affected the length-scale by which leader cells can correlate their forces such that actomyosin contractility levels inversely correlate with the frequency of leader cell formations (***Vishwakarma et al.*** (***2018***)). We propose that altered patterns of PIEZO1-induced retractions within a monolayer may inhibit normal signal transduction by leader cells and disrupt cells from moving cohesively during collective migration. Given that these contractile forces could be communicated through cell-cell adhesions, patterns of cell contractility within the monolayer could be modeled to explore this by incorporating a variable adhesion coefficient in a PDE model or using a discrete approach such as a Vertex Model (***González-Valverde and García-Aznar*** (***2018***); ***Wynn et al.*** (***2013***)).

Since faster wound healing provides several physiological advantages to an organism, the role of PIEZO1 expression in keratinocytes may seem counterintuitive; however, other groups have reported that too many leader cells results in a disorganized epithelial sheet which affects the quality of wound closure (***Omelchenko et al.*** (***2003***)). Recent work examining wound healing in *Drosophila* found that knockout of the *Piezo1* orthologue, *Piezo*, resulted in poorer epithelial patterning and although wounds closed faster, they did so at the expense of epidermal integrity (***Zechini et al.*** (***2022***)). Therefore, it appears that effective wound healing may require a delicate balance of PIEZO1 activity.

PIEZO1 has been found to influence migration in other cell types, but whether channel activity inhibits or promotes cell migration has been seen to vary (***Chubinskiy-Nadezhdin et al.*** (***2019***); ***Huang et al.*** (***2019***); ***Li et al.*** (***2015***); ***Maneshi et al.*** (***2018***); ***Marchant et al.*** (***2022***); ***McHugh et al.*** (***2012***); ***Yu et al.*** (***2021***); ***Zhang et al.*** (***2018***)). Interestingly, recent studies found that PIEZO1 inhibition suppresses collective migration and results in a decrease in the directionality of migrating *Xenopus* neural crest cells (***Canales Coutiño and Mayor*** (***2021***); ***Marchant et al.*** (***2022***)). We note that the tissue-context of collective migration is known to engage distinct spatiotemporal signal transduction pathways (***Friedl and Gilmour*** (***2009***); ***Haeger et al.*** (***2015***); ***Ladoux and Mège*** (***2017***)). Therefore, our seemingly contradictory findings to the observations in neural crest cells could reflect the inherent differences between the migration of neural crest cells and that of keratinocytes during reepithelialization. This highlights the need for studying PIEZO1 mechanotransduction under different biological contexts of cell migration.

Collective cell migration is an emergent phenomenon occuring at the multicellular level and stems from the large-scale coordination of individual cellular motions. Mechanical forces have been highlighted as playing an important role in shaping collective cell behaviors and influencing the formation and dynamics of both leader and follower cells (***Das et al.*** (***2015***); ***Ladoux and Mège*** (***2017***); ***Vishwakarma et al.*** (***2020***)). Through this work, we have identified that PIEZO1 activity suppresses leader cell formation and inhibits the coordination of cellular motion across length scales during keratinocyte collective migration. Moreover, we develop a robust mathematical model for collective cell migration which is generalizable to studying the role of other proteins or cell types during collective keratinocyte migration through analogous simulation and analyses. We propose that elevated PIEZO1-induced cell retraction inhibits the normal long-range coordination between cells during collective migration, disrupting typical mechanochemical activity patterns and the coordinated polarization of neighboring cells. Our findings provide a new biophysical mechanism by which PIEZO1 activity regulates the spatiotemporal dynamics across multiple cells to shape collective migration.

Acknowledgments

We thank Dr. Ardem Patapoutian and his lab for the generous gift of *Piezo1*-cKO and *Piezo1*-GoF keratinocytes. We thank Gabriella Bertaccini for helpful comments on the manuscript.

Grant Support

This work was supported by NIH grants R01NS109810 and DP2AT010376 to MMP; NSF grant DMS-1953410 to JSL; a skin seed grant through 5P30AR075047-03 to MMP and JSL; a James H Gilliam Fellowship for Advanced Study (GT11549) from the Howard Hughes Medical Institute to MMP and JRH, and a seed grant to JRH and JC from the UCI NSF-Simons Center for Multiscale Cell Fate Research (funded by NSF grant DMS1763272 and a Simons Foundation grant 594598).

Methods and Materials

Animals

Keratinocyte samples from *Piezo1*-cKO and *Piezo1*-GoF mice were a gift from Dr. Ardem Patapoutian's lab. *Piezo1*-tdTomato reporter mice (*Piezo1*-tdTomato; JAX stock 029214), *Piezo1*-cKO and *Piezo1*-GoF mice were generated in previous studies (***Holt et al.*** (***2021***); ***Ranade et al.*** (***2014***)). All studies were approved by the Institutional Animal Care and Use Committee of University of California at Irvine and The Scripps Research Institute and performed within their guidelines.

Keratinocyte Isolation and Culture:

Primary keratinocytes were isolated from the upper dorsal skin of P0-P5 mice as previously described (***Holt et al.*** (***2021***)). Briefly, dissected tissue was allowed to dissociate for 15-18 hours. After dissociation, the epidermis was separated and incubated in Accutase (CellnTec CnT-Accutase-100) for 30 minutes at room temperature. Subsequently, the epidermis was transferred to a dish of CnT-Pr media (CellnTec), supplemented with 10% FBS and 1% penicillin/streptomycin where the epidermis was minced and then agitated using a stir plate for 30 min. After agitation, cells were strained through a 70 μm cell strainer (Falcon). Strained cells were spun down and resuspended in CnT-Pr media (CellnTec) supplemented with ISO-50 (1:1000) (CellnTec) and Gentamicin (50 μg/ml) (Thermo Fisher).

Isolated keratinocytes were seeded directly onto the glass region of #1.5 glass-bottom dishes (Mat-Tek Corporation) coated with 10 μg/ml fibronectin (Fisher Scientific, CB-40008A). For single cell migration experiments, isolated cells were sparsely seeded onto the glass region at 1.5×10^4 cells/dish while for monolayer scratch assay experiments, isolated cells were densely seeded onto the glass region at a density of 1.5×10^5 cells/dish. One day after seeding, CnT-Pr supplemented culture media (see above) was switched to Cnt-Pr-D media (CellnTec) to promote keratinocyte differentiation. Keratinocytes were imaged 3 days after primary isolation, allowing at least 2 days for keratinocyte differentiation in Cnt-Pr-D media (CellnTec).

Microscopy:

For *in vitro* image acquisition, an Olympus IX83-ZDC inverted microscope equipped with a SOLA light engine (Lumencor) was utilized. For time-lapse imaging experiments, a full enclosure stage-top incubator system (Tokai Hit) enabled cells to be imaged at 37°C with 5% CO_2 to maintain optimal cell health. μManager, an open-source microscopy controller software, was used for microscope hardware control and image acquisition (***Edelstein et al.*** (***2010***); ***Edelstein et al.*** (***2014***)). For all experimental data, images were taken using a UPlanSApo 10× dry objective with a numerical aperture of 0.40 and acquired using a Hamamatsu Flash 4.0 v2+ scientific CMOS camera.

Single Cell Migration Assay:

As previously described (***Holt et al.*** (***2021***)), time lapse sequences of DIC images were taken at 5 minute intervals. In brief, sparsely seeded keratinocytes were allowed to migrate for 16.67 hr at 37°C with 5% CO_2 in fibronectin-coated glass-bottom dishes. Cell centroids were tracked using Cell Tracker (https://celltracker.website/index.html; ***Piccinini et al.*** (***2016***)) and resulting trajectories were analyzed using the cell trajectory analysis software, DiPer (***Gorelik and Gautreau*** (***2014***)).

Wound Closure assay:

Primary keratinocytes were cultured for 3 days until they formed a confluent monolayer. Prior to imaging experiments, cell nuclei were labeled by addition of SiR-Hoechst (1 μM; (***Lukinavičius et al.*** (***2015***); Cytoskeleton Inc.) to Cnt-Pr-D+1.2 mM Ca^{2+} bath media for 1 hour prior to imaging. As previously described, monolayer scratches were generated using a 10 μl pipette tip and resulting cell debris was removed by performing three successive washes of culturing media (***Holt et al.*** (***2021***); ***Liang et al.*** (***2007***)). Time-lapse imaging series of wound closure were acquired by taking sequential DIC and Cy5 images at multiple positions. 1 μM SiR-Hoechst remained in the Cnt-Pr-D+1.2 mM Ca^{2+} bath media throughout the imaging period. For Yoda1 experiments, 4 μM Yoda1 or, as a control, the equivalent concentration of DMSO was supplemented to bath media prior to imaging. Leader Cells were manually identified from review of time-lapse image series and the number of leader cell formations is reported at the time point when either the wound interfaces touch or the imaging period finishes.

Wound Edge Length Analysis:

Monolayer sheets were segmented from images taken during wound closure assays using a custom deep-learning based U-net architecture written in Python (***Ronneberger et al.*** (***2015***); https://github.com/Pathak-Lab/PIEZO1-Collective-Migration). The length

Figure 6

Figure 6—figure supplement 1. Image processing pipeline for nuclei images.

of the segmented wound edge is calculated by taking the cumulative euclidean distance between all detected pixel positions along the segmented monolayer leading edge. Due to any possible differences in edge length which might arise when manually making scratches in monolayers, each field of view's edge length was normalized by dividing the edge length at T_{final}, the time point when either the wound interfaces touch or the imaging period finishes by T_0, the starting edge length at the starting time point for a field of view. This normalized edge length was used as a measure of the prevalence of leader cells along the wound edge for a given condition.

Image Analysis:

Using the open-source image analysis software Fiji (***Schindelin et al.*** (***2012***)) the signal-to-noise ratio of Sir-Hoechst images was increased using Contrast Limited Adaptive Histogram Equalization (CLAHE) (https://imagej.net/plugins/clahe) prior to further analysis. For some images which had poor labeling of Sir-Hoechst, the denoising algorithm Noise2Void was also used to further increase the signal-to-noise ratio of nuclei images (***Krull et al.*** (***2018***)) (***Figure 6—figure Supplement 1***).

Individual Cell Tracking:

We combined the deep learning network StarDist with the cell tracking software TrackMate to perform automated tracking of cells within monolayers (***Ershov et al.*** (***2022***); ***Fazeli et al.*** (***2020***); ***Tinevez et al.*** (***2017***)). Cell trajectories harvested using Trackmate were then exported for further analysis. Due to the technical limitations surrounding Microsoft Excel's ability to handle large datasets, we developed Cell_Pyper (https://github.com/Pathak-Lab/PIEZO1-Collective-Migration) a Pythonic analysis pipeline based on the open-source algorithm DiPer (***Gorelik and Gautreau*** (***2014***)) to analyze the Mean Squared Displacement (MSD), Speed and Velocity autocorrelation of harvested cell trajectories.

For efficient computation of a trajectory's MSD, MSDs are computed according to Eq. 6 (Eq. 4.11 in ***Calandrini et al.*** (***2011***)) where $r(k) \equiv r(k\Delta t)$ is a cell trajectory consisting of N_t timepoints and the MSD is calculated for timestep m.

$$\Delta^2(m) = \frac{1}{N_t - m} \sum_{k=0}^{N_t-m-1} [r(k+m) - r(k)]^2 \quad m = 0 \ldots N_t - 1 \tag{6}$$

As initially described by Gorelik & Gautreau (Eq. 6 and 7 in (***Gorelik and Gautreau*** (***2014***)), Velocity Autocorrelation analysis is calculated according to equations 7 and 8 for a trajectory consisting of N timepoints with a time-step of Δt=5 min. A normalization factor (Norm; Eq. 7) is initially calculated for velocity vector v_i with starting coordinates (x_i, y_i) which is used to calculate the average velocity autocorrelation coefficient v_{ac} with step size n.

$$\begin{aligned} \text{Norm} &= \frac{1}{N} \Sigma_{i=0}^{N-1} |\bar{v}|_i^2 = \\ &= \frac{1}{N*(\Delta t)^2} \Sigma_{i=0}^{N-1} \left[(x_i - x_{i+1})^2 + (y_i - y_{i+1})^2 \right] \end{aligned} \tag{7}$$

$$\begin{aligned} v_{ac}(n) &= \frac{1}{N-n} \left(\Sigma_{i=0}^{N-n} \bar{v}_i \cdot \bar{v}_{i+n} \right) * \frac{1}{Norm} \\ &= \frac{1}{N-n} \Sigma_{i=0}^{N-n} \left[\frac{(x_i - x_{i+1})(x_{i+n} - x_{i+n+1}) + (y_i - y_{i+1})(y_{i+n} - y_{i+n+1})}{(\Delta t)^2} * \frac{1}{Norm} \right] \end{aligned} \tag{8}$$

Particle Image Velocimetry Analysis:

Particle Image Velocimetry (PIV) analysis is performed using the Python implementation of OpenPIV (***Liberzon et al.*** (***2020***); https://github.com/Pathak-Lab/PIEZO1-Collective-Migration). We use multiple passes of interrogation window sizes, initially using first-pass calculations with a 64 pixel x 64 pixel (55.2 μm x 55.2 μm) window followed by two iterations of 32 x 32 (27.6 μm x 27.6 μm) pixel windows and two iterations of 16 x 16 pixel (13.8 μm x 13.8 μm) windows. Each interrogation window was computed with a 50% overlap. A signal-to-noise filter (Threshold=1.3) was used on detected velocity vectors to remove any vector outliers. Outputs produced by OpenPIV analysis were then used to generate PIV flow fields as shown in ***Figure 5A-C***. Working from the flow fields, individual PIV vectors were isolated and PIV vector direction was calculated and normalized to 0° to account for differences in angles

of scratches made in monolayers (https://github.com/Pathak-Lab/PIEZO1-Collective-Migration). Vector direction distributions are illustrated as the cumulative frequency distribution across experimental replicates in ***Figure 5D-F***.

The variance of PIV vector directions within a field of view was calculated as the mean angular deviation, *z*, where *z* is defined in Eq. 9 (Eq. 2 in ***Lee et al.*** (***2016***)). Outputs of this equation are bounded such that zero indicates no variability in vector direction within a flow field and one indicates high variability in vector direction.

$$z = \frac{1}{N}\left[\left(\sum_{i}^{N}\cos\theta_i\right)^2 + \left(\sum_{i}^{N}\sin\theta_i\right)^2\right]^{1/2} \tag{9}$$

The spatial autocorrelation function, C , is computed according to Eq. 10 (Eq. 4 in ***Lee et al.*** (***2016***)) using the radial velocity component of a given PIV vector, *v*, within a vector flow field at varying length scales, *r*.

$$C(\Delta r) = \frac{\Sigma_{r_i} v\left(r_i\right)\cdot v\left(r_i+\Delta r\right)}{\sqrt{\Sigma_{r_i} v_i^2\left(r_i\right)\cdot \Sigma_{r_i} v^2\left(r_i+\Delta r\right)}} \tag{10}$$

For measurement of the local autocorrelation in vector direction, the spatial autocorrelation at Δr = 150 μm was used to capture correlation of motion at multiple cell lengths. Length constants were calculated by fitting an exponential function whose exponent is a 2nd order polynomial(Eq. 11) to the spatial autocorrelation dataset and calculating the distance at which $C(\Delta r) \approx 0.37$.

$$y = e^{a+bx+cx^2} \tag{11}$$

Multi-scale Modeling: from Discrete Model to Continuum Limit

In the discrete master equation (Eq. 1), $T^{\rightarrow}_{i,j}$ the transitional probability for cells traveling from $x_{i,j}$ to $x_{i+1,j}$ is defined as the following:

$$T^{\rightarrow}_{i,j} = (1-\rho_{i+1,j})(1-\alpha\rho_{i-1,j})(1-\alpha\rho_{i,j+1})(1-\alpha\rho_{i,j-1})(f^{\rightarrow}_{i,j} + b^{\rightarrow}_{i,j}). \tag{12}$$

The term $(1-\rho_{i+1,j})$ models the effects of volume filling and $(1-\alpha\rho_{i-1,j})(1-\alpha\rho_{i,j+1})(1-\alpha\rho_{i,j-1})$ models cell-cell adhesion from 3 directions hindering the cell migration, where $\alpha \in [0,1]$ is the adhesion coefficient (***Anguige and Schmeiser*** (***2008***)). In the last term $f^{\rightarrow}_{i,j} + b^{\rightarrow}_{i,j}$, the vector $f^{\rightarrow}_{i,j} = d^{\leftrightarrow}\rho_{i,j}/h^2$ models diffusive cell motion while $b^{\rightarrow}_{i,j} = r^{\rightarrow}_{i,j}/h$ models cell movement due to retraction. The dependence on h reflects diffusive ($\mathcal{O}(1/h^2)$) and advective scaling of the equations ($\mathcal{O}(1/h)$), respectively (see Appendix 1 Section 4 for details). Further, $d^{\leftrightarrow}$ is the directional cell motility, while $r^{\rightarrow}_{i,j}$ accounts for the retraction of the cell. In particular, $r^{\leftarrow}_{i,j} = r^{\rightarrow}_{i,j} = \bar{r}$ if there is no retraction at $x_{i,j}$, e.g., monolayer region far away behind the wound edge. In this case, the governing equation is a pure diffusion equation without advection (Eq. 23) since $\Delta r^{\leftrightarrow} = r^{\leftarrow} - r^{\rightarrow} = 0$, which appears in the continuum limit. In the retraction region, $r^{\leftarrow}_{i,j}$ increases and $r^{\rightarrow}_{i,j}$ decreases, so $\Delta r^{\leftrightarrow} = r^{\leftarrow} - r^{\rightarrow} \neq 0$ and the governing equation turns into a diffusion-advection equation (Eq. 22). Note that the cell density term $\rho_{i,j}$ in $f^{\rightarrow}_{i,j}$ models the moving front that connects a zero-density region (wound) with a non-zero density region (monolayer), e.g. (***Witelski et al.*** (***1995***)). The other transitional probabilities $T^{\leftarrow}_{i,j}$, $T^{\uparrow}_{i,j}$, $T^{\downarrow}_{i,j}$ can be defined analogously. Hence, Eq. 12 can be rewritten as

$$\begin{aligned} T^{\rightarrow}_{i,j} =& \frac{(1-\rho_{i+1,j})(1-\alpha\rho_{i-1,j})(1-\alpha\rho_{i,j+1})(1-\alpha\rho_{i,j-1})d^{\leftrightarrow}\rho_{i,j}}{h^2} \\ &+ \frac{(1-\rho_{i+1,j})(1-\alpha\rho_{i-1,j})(1-\alpha\rho_{i,j+1})(1-\alpha\rho_{i,j-1})r^{\rightarrow}_{i,j}}{h}. \end{aligned} \tag{13}$$

Recall that cell directionality refers to the process in which cells receive information to move toward the direction of the wound gap, i.e., in the y direction in our experimental configuration, so cells are assumed to have a larger directional mobility in the y direction, i.e., $d^{\updownarrow} \geq d^{\leftrightarrow}$. Hence, the following decomposition holds:

$$
\begin{aligned}
\begin{pmatrix} d^{\leftrightarrow} & 0 \\ 0 & d^{\updownarrow} \end{pmatrix} &= d^{\updownarrow} \cdot \begin{pmatrix} \frac{d^{\leftrightarrow}}{d^{\updownarrow}} & 0 \\ 0 & 1 \end{pmatrix} = d^{\updownarrow} \cdot \begin{pmatrix} \frac{d^{\leftrightarrow}}{d^{\updownarrow}} & 0 \\ 0 & \frac{d^{\leftrightarrow}}{d^{\updownarrow}} + \frac{d^{\updownarrow}-d^{\leftrightarrow}}{d^{\updownarrow}} \end{pmatrix} \\
&= d^{\updownarrow} \cdot \left(\begin{pmatrix} \frac{d^{\leftrightarrow}}{d^{\updownarrow}} & 0 \\ 0 & \frac{d^{\leftrightarrow}}{d^{\updownarrow}} \end{pmatrix} + \begin{pmatrix} 0 & 0 \\ 0 & \frac{d^{\updownarrow}-d^{\leftrightarrow}}{d^{\updownarrow}} \end{pmatrix} \right) \\
&= d^{\updownarrow} \cdot \left(\frac{d^{\leftrightarrow}}{d^{\updownarrow}} \cdot \begin{pmatrix} 1 & 0 \\ 0 & 1 \end{pmatrix} + \frac{d^{\updownarrow} - d^{\leftrightarrow}}{d^{\updownarrow}} \cdot \begin{pmatrix} 0 & 0 \\ 0 & 1 \end{pmatrix} \right) \\
&= d \cdot (w_I \boldsymbol{I} + w_A \boldsymbol{A})
\end{aligned} \tag{14}
$$

by defining the coefficients of cell motility d, isotropic strength w_I and anisotropic strength w_A (cell directionality):

$$
\begin{aligned}
d &= d^{\updownarrow}, \\
w_I &= \frac{d^{\leftrightarrow}}{d^{\updownarrow}}, \\
w_A &= \frac{d^{\updownarrow} - d^{\leftrightarrow}}{d^{\updownarrow}},
\end{aligned} \tag{15}
$$

where the directionality assumption $d^{\updownarrow} \geq d^{\leftrightarrow}$ guarantees the weights w_I and w_A are non-negative and bounded by 1, and the convex weighting relation $w_I + w_A = 1$ naturally holds from the derivation of w_I and w_A. From the relations above, we can see how w_A measures cell directionality: cells under a stronger directionality are more likely to migrate towards the direction of closure, which increases the difference between $d^{\updownarrow}$ and $d^{\leftrightarrow}$, consequently increasing w_A to weight the diffusion anisotropy $\boldsymbol{A}$ more than the diffusion isotropy $\boldsymbol{I}$. In contrast, $w_I = d^{\leftrightarrow}/d^{\updownarrow}$ is a ratio indicating the randomness of cell migration directionality, but we only focus on w_A since $w_I = 1 - w_A$ is determined by w_A.

By taking $h \to 0$, the continuum limit (Eq. 2) is obtained from the discrete master equation (Eq. 1), where the diffusivity $\boldsymbol{D} = d \cdot (w_I \boldsymbol{I} + w_A \boldsymbol{A}) \cdot \hat{D}_\alpha(\rho)$ (Eq. 3) of the continuous equation is derived from $f_{i,j}^{\rightarrow}$, $f_{i,j}^{\leftarrow}$, $f_{i,j}^{\uparrow}$ and $f_{i,j}^{\downarrow}$ in the transitional probabilities (Eq. 12): $d \cdot (w_I \boldsymbol{I} + w_A \boldsymbol{A})$ comes from $d^{\updownarrow}$ and $d^{\leftrightarrow}$, while the scalar diffusion coefficient $\hat{D}_\alpha(\rho)$ takes the following form:

$$
\hat{D}_\alpha(\rho) = 2\rho - (1 + 11\alpha)\rho^2 + (8\alpha + 16\alpha^2)\rho^3 - (13\alpha^2 + 7\alpha^3)\rho^4 + 6\alpha^3\rho^5, \tag{16}
$$

which is derived from the scaled cell density $\rho_{i,j}/h^2$, cell-cell adhesion (e.g., $(1-\alpha\rho_{i-1,j})(1-\alpha\rho_{i,j+1})(1-\alpha\rho_{i,j-1})$ in $f_{i,j}^{\rightarrow}$) and volume filling (e.g., $1 - \rho_{i+1,j}$ in $f_{i,j}^{\rightarrow}$).

Retraction localization:

Following the localization assumptions (1) (2), a choice for $\Delta r^{\leftrightarrow}$ and $\Delta r^{\updownarrow}$ is:

$$
\Delta r^{\leftrightarrow} = \Delta r^{\updownarrow} = \tilde{H}(\gamma - \rho) \cdot \sum_{i=1}^{\infty} s_i \cdot \mathbb{1}_{[\tau_i, \tau_i + \mathcal{T}_i^r)}(t) \cdot \tilde{\mathbb{1}}_{\Omega_i}(\mathbf{x}), \tag{17}
$$

where H is a Heaviside function

$$
H(\gamma - \rho) = \begin{cases} 1 & , \rho < \gamma \\ 0 & , \rho \geq \gamma \end{cases} \tag{18}
$$

with threshold γ, which localizes the retraction to the wound edge ($\gamma = 0.4$ was adapted in the simulation). In particular, $H(\gamma - \rho) = 0$ turns off the retraction for $\rho > \gamma$, which is the high cell density region far away from the wound edge, while $H(\gamma - \rho) = 1$ turns on the retraction for $\rho < \gamma$, which is the low cell density region near the wound edge.

By labeling retraction events in chronological order with positive integers $i = 1, 2, 3, \ldots$, indicator functions $\mathbb{1}_{[\tau_i, \tau_i + \mathcal{T}_i^r)}(t)$ and $\mathbb{1}_{\Omega_i}(\mathbf{x})$ localize the regions where the edge retracts in time and space, respectively. We take the retraction to be localized in a region $\Omega_i := [c_i - \omega_r/2, c_i + \omega_r/2] \times [0, 1]$ about a line segment $x = c_i$ with width ω_r ($\omega_r = 0.2$ was used in the simulation)

$$
\mathbb{1}_{\Omega_i}(\mathbf{x}) = \mathbb{1}_{[c_i - \omega_r/2, c_i + \omega_r/2]}(x) = \begin{cases} 1 & , |x - c_i| \leq \omega_r/2 \\ 0 & , \text{otherwise} \end{cases} \tag{19}
$$

where we account for randomness by taking the uniform distribution $c_i \sim \mathcal{U}(0, 1)$. This allows the region Ω_i to randomly slide around $[0, 1]$ to localize the retraction events.

The retractions are assumed to occur at particular times τ_i with durations $\mathcal{T}_i^r$. Accordingly, we take

$$s_i \cdot \mathbb{1}_{[\tau_i, \tau_i + \mathcal{T}_i^r)}(t) = \begin{cases} s_i & , \tau_i \leq t < \tau_i + \mathcal{T}_i^r \\ 0 & , \text{otherwise} \end{cases} \tag{20}$$

where s_i is the speed (or strength) of the retraction, and the next retraction occurs at $\tau_{i+1} = \tau_i + \mathcal{T}_i^r + \mathcal{T}_i^{nr}$ with the inter-retraction (no retraction) duration $\mathcal{T}_i^{nr}$. To account for randomness, we assume

$$\mathcal{T}_i^r \overset{iid}{\sim} \mathcal{N}(\mu_r, \sigma_r^2) \quad \perp\!\!\!\perp \quad \mathcal{T}_i^{nr} \overset{iid}{\sim} \mathcal{N}(\mu_{nr}, \sigma_{nr}^2) \quad \perp\!\!\!\perp \quad s_i \overset{iid}{\sim} \mathcal{N}(\mu_s, \sigma_s^2) \tag{21}$$

where $\mathcal{N}(\mu, \sigma^2)$ denotes the normal distribution with mean μ and standard deviation σ, and all random variables are independent and identically distributed (iid).

In summary, $\Delta r^{\leftrightarrow}$ and $\Delta r^{\updownarrow}$ are designed to model retractions such that cell movement would be governed by a diffusion-advection equation that guides the migrating cells in the retraction region near the wound edge:

$$\frac{\partial \rho}{\partial t} = \nabla \cdot (\boldsymbol{D} \nabla \rho) + \nabla \cdot (\boldsymbol{s}(1-\rho)(1-\alpha\rho)^3 \rho) \quad \text{near wound edge} \tag{22}$$

where $\boldsymbol{D}$ is the diffusivity (Eq. 3) and $\boldsymbol{s} = (s, s)^T / \sqrt{2}$ where the retraction strength, s, regulates the magnitude of advection velocity. On the other hand, cells far from the wound edge (e.g., interior of the monolayer) migrate following a simple diffusion equation

$$\frac{\partial \rho}{\partial t} = \nabla \cdot (\boldsymbol{D} \nabla \rho) \quad \text{away from wound edge} \tag{23}$$

with the same diffusivity (Eq. 3).

Note that both Heaviside function $H(\gamma - \rho)$ and characteristic function $\mathbb{1}_{\Omega_i}(\mathbf{x})$ are discontinuous. To preserve differentiability, we smooth H using a hyperbolic tangent function $\tilde{H}$ (Eq. 31 in Appendix 1 Section 5) and smooth $\mathbb{1}_{\Omega_i}(\mathbf{x})$ using a generalized bell-shaped function $\tilde{\mathbb{1}}_{\Omega_i}(\mathbf{x})$ (Eq. 32 in Appendix 1 Section 5). Since the definition of $\Delta r^{\leftrightarrow}$ and $\Delta r^{\updownarrow}$ (Eq. 17) given above is not the only way to interpolate the advection velocity between the retraction region and the regions that do not retract, and other choices could be used. However, the qualitative results of the model are not sensitive to the choice of $\Delta r^{\leftrightarrow}$ and $\Delta r^{\updownarrow}$ under assumptions (1) and (2) and reduction of the equations to (Eq. 22, Eq. 23) near and far from the wound edge.

Numerical scheme:

In order to solve the governing equation (Eq. 2), we firstly carry out an forward time discretization (with size Δt) on the left hand side $\partial \rho / \partial t$ by $(\rho(\boldsymbol{x}_{i,j}, t + \Delta t) - \rho(\boldsymbol{x}_{i,j}, t))/\Delta t$. In terms of space discretization (right hand side), the transitional probability is proved to be separable (Eq. 13) in the discrete model, which allows us to work on the diffusion part and advection part separately: for the diffusion part, a natural discretization is directly given by the discrete model (e.g., centered finite differences); for the advection part, we apply a 2nd order weighted essentially non-oscillatory (WENO) method (***Jiang and Shu*** (***1996***); ***Liu et al.*** (***1994***)) to discretize the equation. Hence, an explicit finite difference scheme was used to update the cell density at the nth time step $\rho_{i,j}^n$ iteratively on the simulation domain $[0, 1] \times [0, 1]$ until wound closure.

Model parameter adjustment:

In ***Figure 3B-D*** and ***Figure 3—figure Supplement 3***, the experimentally derived "Single Cell Migration" dataset guides the changes in model parameters of retraction strength, retraction duration, inter-retraction duration and cell motility when PIEZO1 activity is altered. However, cell-cell adhesion and cell directionality were not measured directly in the experiments and instead are inferred by trying to match model and experimental results.

While both cell-cell adhesion and cell directionality are designed to range from 0 to 1 in our model, the feasible adhesion coefficient actually needs to be bounded above by 0.66 in order for the diffusivity to be positive definite (see Appendix 1 section 3 for detailed derivation). Since the dependence of wound closure rate and wound edge length with respect to individual model parameters was already numerically shown to be a monotone function of these parameters (***Figure 2G, H*** and ***Figure 2—figure Supplement 2***), it is sufficient to directly use the extrema of the model parameters: 1 for increased directionality, 0.66 for an increased adhesion, and 0 in the case that directionality and/or adhesion is decreased. For example, when matching experiments and simulations requires an increased directionality, we take $w_A = 1$. Because of the dependency of the outcomes (wound closure rate and edge lengths), if increasing a model parameter to its maxima fails to match the experimental trends, it would be impossible to match with smaller values.

The base values of cell-cell adhesion and cell directionality are taken to be 0.2 and 0.4, respectively. In ***Figure 2B-D***, the adhesion coefficient is fixed at the value 0.2, while in ***Figure 3—figure Supplement 3***, cell directionality is fixed at the value 0.4.

Statistical analysis:

Sample sizes are declared in the corresponding figures. Cumming estimation plots were generated and Cohen's *d* value was calculated using the DABEST python (***Ho et al.*** (***2019***)) (https://github.com/ACCLAB/DABEST-python). *p* values for ***Figure 2G-I*** are declared in ***Figure 5—figure Supplement 2***.

Code Availability:

All code used to analyze datasets has been made publicly available (https://github.com/Pathak-Lab/PIEZO1-Collective-Migration).

References

Angelini TE, Hannezo E, Trepat X, Fredberg JJ, Weitz DA. Cell migration driven by cooperative substrate deformation patterns. Phys Rev Lett. 2010 Apr; 104(16):168104.

Angelini TE, Hannezo E, Trepat X, Marquez M, Fredberg JJ, Weitz DA. Glass-like dynamics of collective cell migration. Proc Natl Acad Sci U S A. 2011 Mar; 108(12):4714–4719.

Anguige K, Schmeiser C. A one-dimensional model of cell diffusion and aggregation, incorporating volume filling and cell-to-cell adhesion. J Math Biol. 2008 Jun; 58(3):395–427.

Bajpai S, Prabhakar R, Chelakkot R, Inamdar MM. Role of cell polarity dynamics and motility in pattern formation due to contact-dependent signalling. J R Soc Interface. 2021 Feb; 18(175):20200825.

Banerjee S, Cristina M. Continuum Models of Collective Cell Migration. Cell Migrations: Causes and Functions. 2019; p. 45–66.

Barry DJ, Durkin CH, Abella JV, Way M. Open source software for quantification of cell migration, protrusions, and fluorescence intensities. J Cell Biol. 2015 Apr; 209(1):163–180.

Bianco A, Poukkula M, Cliffe A, Mathieu J, Luque CM, Fulga TA, Rørth P. Two distinct modes of guidance signalling during collective migration of border cells. Nature. 2007 Jul; 448(7151):362–365.

Boocock D, Hino N, Ruzickova N, Hirashima T, Hannezo E. Theory of mechanochemical patterning and optimal migration in cell monolayers. Nat Phys. 2020 Sep; 17(2):267–274.

Buttenschön A, Edelstein-Keshet L. Bridging from single to collective cell migration: A review of models and links to experiments. PLoS Comput Biol. 2020 Dec; 16(12):e1008411.

Cai D, Chen SC, Prasad M, He L, Wang X, Choesmel-Cadamuro V, Sawyer JK, Danuser G, Montell DJ. Mechanical feedback through E-cadherin promotes direction sensing during collective cell migration. Cell. 2014 May; 157(5):1146–1159.

Calandrini V, Pellegrini E, Calligari P, Hinsen K, Kneller GR. nMoldyn - Interfacing spectroscopic experiments, molecular dynamics simulations and models for time correlation functions. Éc thémat Soc Fr Neutron. 2011; 12:201–232.

Canales Coutiño B, Mayor R. The mechanosensitive channel Piezo1 cooperates with semaphorins to control neural crest migration. Development. 2021 Dec; 148(23).

Capuana L, Boström A, Etienne-Manneville S. Multicellular scale front-to-rear polarity in collective migration. Curr Opin Cell Biol. 2020 Feb; 62:114–122.

Chubinskiy-Nadezhdin VI, Vasileva VY, Vassilieva IO, Sudarikova AV, Morachevskaya EA, Negulyaev YA. Agonist-induced Piezo1 activation suppresses migration of transformed fibroblasts. Biochem Biophys Res Commun. 2019 Jun; 514(1):173–179.

Das T, Safferling K, Rausch S, Grabe N, Boehm H, Spatz JP. A molecular mechanotransduction pathway regulates collective migration of epithelial cells. Nat Cell Biol. 2015 Mar; 17(3):276–287.

Dean ZS, Jamilpour N, Slepian MJ, Wong PK. Decreasing Wound Edge Stress Enhances Leader Cell Formation during Collective Smooth Muscle Cell Migration. ACS Biomater Sci Eng. 2019 Aug; 5(8):3864–3875.

Deforet M, Hakim V, Yevick HG, Duclos G, Silberzan P. Emergence of collective modes and tri-dimensional structures from epithelial confinement. Nat Commun. 2014 May; 5:3747.

Doxzen K, Vedula SRK, Leong MC, Hirata H, Gov NS, Kabla AJ, Ladoux B, Lim CT. Guidance of collective cell migration by substrate geometry. Integr Biol. 2013 Aug; 5(8):1026–1035.

Edelstein A, Amodaj N, Hoover K, Vale R, Stuurman N. Computer control of microscopes using μManager. Curr Protoc Mol Biol. 2010 Oct; Chapter 14:Unit14.20.

Edelstein AD, Tsuchida MA, Amodaj N, Pinkard H, Vale RD, Stuurman N. Advanced methods of microscope control using μManager software. J Biol Methods. 2014; 1(2).

Ershov D, Phan MS, Pylvänäinen JW, Rigaud SU, Le Blanc L, Charles-Orszag A, Conway JRW, Laine RF, Roy NH, Bonazzi D, Duménil G, Jacquemet G, Tinevez JY. TrackMate 7: integrating state-of-the-art segmentation algorithms into tracking pipelines. Nat Methods. 2022 Jun; p. 1–4.

Fazeli E, Roy NH, Follain G, Laine RF, von Chamier L, Hänninen PE, Eriksson JE, Tinevez JY, Jacquemet G. Automated cell tracking using StarDist and TrackMate. F1000Res. 2020 Oct; 9:1279.

Franz CM, Jones GE, Ridley AJ. Cell migration in development and disease. Dev Cell. 2002 Feb; 2(2):153–158.

Friedl P, Gilmour D. Collective cell migration in morphogenesis, regeneration and cancer. Nat Rev Mol Cell Biol. 2009 Jul; 10(7):445–457.

González-Valverde I, García-Aznar JM. Mechanical modeling of collective cell migration: An agent-based and continuum material approach. Comput Methods Appl Mech Eng. 2018 Aug; 337:246–262.

Gorelik R, Gautreau A. Quantitative and unbiased analysis of directional persistence in cell migration. Nat Protoc. 2014 Aug; 9(8):1931–1943.

Haeger A, Wolf K, Zegers MM, Friedl P. Collective cell migration: guidance principles and hierarchies. Trends Cell Biol. 2015 Sep; 25(9):556–566.

Hakim V, Silberzan P. Collective cell migration: a physics perspective. Rep Prog Phys. 2017 Jul; 80(7):076601.

Hino N, Rossetti L, Marín-Llauradó A, Aoki K, Trepat X, Matsuda M, Hirashima T. ERK-Mediated Mechanochemical Waves Direct Collective Cell Polarization. Dev Cell. 2020 Jun; 53(6):646–660.e8.

Ho J, Tumkaya T, Aryal S, Choi H, Claridge-Chang A. Moving beyond P values: data analysis with estimation graphics. Nat Methods. 2019 Jul; 16(7):565–566.

Holmes WR, Park J, Levchenko A, Edelstein-Keshet L. A mathematical model coupling polarity signaling to cell adhesion explains diverse cell migration patterns. PLoS Comput Biol. 2017 May; 13(5):e1005524.

Holt JR, Zeng WZ, Evans EL, Woo SH, Ma S, Abuwarda H, Loud M, Patapoutian A, Pathak MM. Spatiotemporal dynamics of PIEZO1 localization controls keratinocyte migration during wound healing. Elife. 2021 Sep; 10.

Huang Z, Sun Z, Zhang X, Niu K, Wang Y, Zheng J, Li H, Liu Y. Loss of stretch-activated channels, PIEZOs, accelerates non-small cell lung cancer progression and cell migration. Biosci Rep. 2019 Mar; 39(3).

Jiang GS, Shu CW. Efficient Implementation of Weighted ENO Schemes. J Comput Phys. 1996 Jun; 126(1):202–228.

Khain E, Katakowski M, Hopkins S, Szalad A, Zheng X, Jiang F, Chopp M. Collective behavior of brain tumor cells: The role of hypoxia. Phys Rev E. 2011 Mar; 83(3):031920.

Khataee H, Czirok A, Neufeld Z. Multiscale modelling of motility wave propagation in cell migration. Sci Rep. 2020 May; 10(1):8128.

Kirfel G, Herzog V. Migration of epidermal keratinocytes: mechanisms, regulation, and biological significance. Protoplasma. 2004 Jun; 223(2-4):67–78.

Ko JM, Lobo D. Continuous Dynamic Modeling of Regulated Cell Adhesion: Sorting, Intercalation, and Involution. Biophys J. 2019 Dec; 117(11):2166–2179.

Krull A, Buchholz TO, Jug F. Noise2Void - Learning Denoising from Single Noisy Images. arXiv:181110980 [cs]. 2018 Nov; .

Lacroix JJ, Botello-Smith WM, Luo Y. Probing the gating mechanism of the mechanosensitive channel Piezo1 with the small molecule Yoda1. Nat Commun. 2018; 9(1).

Ladoux B, Mège RM. Mechanobiology of collective cell behaviours. Nat Rev Mol Cell Biol. 2017 Dec; 18(12):743–757.

Lee RM, Stuelten CH, Parent CA, Losert W. Collective cell migration over long time scales reveals distinct phenotypes. Converg Sci Phys Oncol. 2016 Jun; 2(2).

Lee RM, Vitolo MI, Losert W, Martin SS. Distinct roles of tumor associated mutations in collective cell migration. Sci Rep. 2021 May; 11(1):10291.

Li C, Rezania S, Kammerer S, Sokolowski A, Devaney T, Gorischek A, Jahn S, Hackl H, Groschner K, Windpassinger C, Malle E, Bauernhofer T, Schreibmayer W. Piezo1 forms mechanosensitive ion channels in the human MCF-7 breast cancer cell line. Sci Rep. 2015 Feb; 5:8364.

Li D, Wang YL. Coordination of cell migration mediated by site-dependent cell-cell contact. Proc Natl Acad Sci U S A. 2018 Oct; 115(42):10678–10683.

Li L, Hartley R, Reiss B, Sun Y, Pu J, Wu D, Lin F, Hoang T, Yamada S, Jiang J, Zhao M. E-cadherin plays an essential role in collective directional migration of large epithelial sheets. Cell Mol Life Sci. 2012 Aug; 69(16):2779–2789.

Liang CC, Park AY, Guan JL. In vitro scratch assay: a convenient and inexpensive method for analysis of cell migration in vitro. Nat Protoc. 2007; 2(2):329–333.

Liberzon A, Lasagna D, Aubert M, Bachant P, Käufer T, jakirkham, Bauer A, Vodenicharski B, Dallas C, Borg J, tomerast, ranleu, OpenPIV/openpiv-python: OpenPIV - Python (v0.22.2) with a new extended search PIV grid option; 2020.

Liu XD, Osher S, Chan T. Weighted Essentially Non-oscillatory Schemes. J Comput Phys. 1994 Nov; 115(1):200–212.

Lukinavičius G, Blaukopf C, Pershagen E, Schena A, Reymond L, Derivery E, Gonzalez-Gaitan M, D'Este E, Hell SW, Wolfram Gerlich D, Johnsson K. SiR-Hoechst is a far-red DNA stain for live-cell nanoscopy. Nat Commun. 2015 Oct; 6:8497.

Maneshi MM, Ziegler L, Sachs F, Hua SZ, Gottlieb PA. Enantiomeric Aβ peptides inhibit the fluid shear stress response of PIEZO1. Sci Rep. 2018 Sep; 8(1):14267.

Marchant CL, Malmi-Kakkada AN, Espina JA, Barriga EH. Cell clusters softening triggers collective cell migration in vivo. Nat Mater. 2022 Aug; .

Mayor R, Etienne-Manneville S. The front and rear of collective cell migration. Nat Rev Mol Cell Biol. 2016 Feb; 17(2):97–109.

McHugh BJ, Murdoch A, Haslett C, Sethi T. Loss of the Integrin-Activating Transmembrane Protein Fam38A (Piezo1) Promotes a Switch to a Reduced Integrin-Dependent Mode of Cell Migration. PLoS One. 2012 Jul; 7(7):e40346.

Oelz D, Khataee H, Czirok A, Neufeld Z. Polarization wave at the onset of collective cell migration. Phys Rev E. 2019 Sep; 100(3-1):032403.

Omelchenko T, Vasiliev JM, Gelfand IM, Feder HH, Bonder EM. Rho-dependent formation of epithelial "leader" cells during wound healing. Proc Natl Acad Sci U S A. 2003 Sep; 100(19):10788–10793.

Petitjean L, Reffay M, Grasland-Mongrain E, Poujade M, Ladoux B, Buguin A, Silberzan P. Velocity fields in a collectively migrating epithelium. Biophys J. 2010 May; 98(9):1790–1800.

Piccinini F, Kiss A, Horvath P. CellTracker (not only) for dummies. Bioinformatics. 2016 Mar; 32(6):955–957.

Poujade M, Grasland-Mongrain E, Hertzog A, Jouanneau J, Chavrier P, Ladoux B, Buguin A, Silberzan P. Collective migration of an epithelial monolayer in response to a model wound. Proc Natl Acad Sci U S A. 2007 Oct; 104(41):15988–15993.

Ranade SS, Qiu Z, Woo SH, Hur SS, Murthy SE, Cahalan SM, Xu J, Mathur J, Bandell M, Coste B, Li YSJ, Chien S, Patapoutian A. Piezo1, a mechanically activated ion channel, is required for vascular development in mice. Proc Natl Acad Sci U S A. 2014 Jul; 111(28):10347–10352.

Reffay M, Parrini MC, Cochet-Escartin O, Ladoux B, Buguin A, Coscoy S, Amblard F, Camonis J, Silberzan P. Interplay of RhoA and mechanical forces in collective cell migration driven by leader cells. Nat Cell Biol. 2014 Mar; 16(3):217–223.

Riahi R, Sun J, Wang S, Long M, Zhang DD, Wong PK. Notch1-Dll4 signalling and mechanical force regulate leader cell formation during collective cell migration. Nat Commun. 2015 Mar; 6:6556.

Ridley AJ, Schwartz MA, Burridge K, Firtel RA, Ginsberg MH, Borisy G, Parsons JT, Horwitz AR. Cell migration: integrating signals from front to back. Science. 2003 Dec; 302(5651):1704–1709.

Ronneberger O, Fischer P, Brox T. U-Net: Convolutional Networks for Biomedical Image Segmentation. In: *Medical Image Computing and Computer-Assisted Intervention – MICCAI 2015* Springer International Publishing; 2015. p. 234–241.

Schindelin J, Arganda-Carreras I, Frise E, Kaynig V, Longair M, Pietzsch T, Preibisch S, Rueden C, Saalfeld S, Schmid B, Tinevez JY, White DJ, Hartenstein V, Eliceiri K, Tomancak P, Cardona A. Fiji: an open-source platform for biological-image analysis. Nat Methods. 2012 Jun; 9(7):676–682.

Seetharaman S, Etienne-Manneville S. Cytoskeletal Crosstalk in Cell Migration. Trends Cell Biol. 2020 Sep; 30(9):720–735.

SenGupta S, Parent CA, Bear JE. The principles of directed cell migration. Nat Rev Mol Cell Biol. 2021 Aug; 22(8):529–547.

Serra-Picamal X, Conte V, Vincent R, Anon E, Tambe DT, Bazellieres E, Butler JP, Fredberg JJ, Trepat X. Mechanical waves during tissue expansion. Nat Phys. 2012 Jul; 8(8):628–634.

Syeda R, Xu J, Dubin AE, Coste B, Mathur J, Huynh T, Matzen J, Lao J, Tully DC, Engels IH, Petrassi HM, Schumacher AM, Montal M, Bandell M, Patapoutian A. Chemical activation of the mechanotransduction channel Piezo1. eLife Sciences. 2015 May; 4:e07369.

Tambe DT, Hardin CC, Angelini TE, Rajendran K, Park CY, Serra-Picamal X, Zhou EH, Zaman MH, Butler JP, Weitz DA, Fredberg JJ, Trepat X. Collective cell guidance by cooperative intercellular forces. Nat Mater. 2011 Jun; 10(6):469–475.

Thompson RN, Yates CA, Baker RE. Modelling Cell Migration and Adhesion During Development. Bull Math Biol. 2012 Oct; 74(12):2793–2809.

Tinevez JY, Perry N, Schindelin J, Hoopes GM, Reynolds GD, Laplantine E, Bednarek SY, Shorte SL, Eliceiri KW. TrackMate: An open and extensible platform for single-particle tracking. Methods. 2017 Feb; 115:80–90.

Trepat X, Wasserman MR, Angelini TE, Millet E, Weitz DA, Butler JP, Fredberg JJ. Physical forces during collective cell migration. Nat Phys. 2009 Jun; 5(6):426–430.

Vedula SRK, Leong MC, Lai TL, Hersen P, Kabla AJ, Lim CT, Ladoux B. Emerging modes of collective cell migration induced by geometrical constraints. Proc Natl Acad Sci U S A. 2012 Aug; 109(32):12974–12979.

Venhuizen JH, Zegers MM. Making Heads or Tails of It: Cell-Cell Adhesion in Cellular and Supracellular Polarity in Collective Migration. Cold Spring Harb Perspect Biol. 2017 Nov; 9(11).

Vicente-Manzanares M, Horwitz AR. Cell migration: an overview. Methods Mol Biol. 2011; 769:1–24.

Vishwakarma M, Di Russo J, Probst D, Schwarz US, Das T, Spatz JP. Mechanical interactions among followers determine the emergence of leaders in migrating epithelial cell collectives. Nat Commun. 2018 Aug; 9(1):3469.

Vishwakarma M, Spatz JP, Das T. Mechanobiology of leader-follower dynamics in epithelial cell migration. Curr Opin Cell Biol. 2020 Oct; 66:97–103.

Wang J, Jiang J, Yang X, Zhou G, Wang L, Xiao B. Tethering Piezo channels to the actin cytoskeleton for mechanogating via the cadherin-β-catenin mechanotransduction complex. Cell Rep. 2022 Feb; 38(6):110342.

Weijer CJ. Collective cell migration in development. J Cell Sci. 2009 Sep; 122(Pt 18):3215–3223.

Witelski TP, Cohen DS, California Institute of Technology Division of Engineering and Applied Science. Problems in Nonlinear Diffusion; 1995.

Wynn ML, Rupp P, Trainor PA, Schnell S, Kulesa PM. Follow-the-leader cell migration requires biased cell-cell contact and local microenvironmental signals. Phys Biol. 2013 Jun; 10(3):035003.

Yang Y, Levine H. Leader-cell-driven epithelial sheet fingering. Phys Biol. 2020 Jul; 17(4):046003.

Yu Y, Wu X, Liu S, Zhao H, Li B, Zhao H, Feng X. Piezo1 regulates migration and invasion of breast cancer cells via modulating cell mechanobiological properties. Acta Biochim Biophys Sin. 2021 Jan; 53(1):10–18.

Zechini L, Amato C, Scopelliti A, Wood W. Piezo acts as a molecular brake on wound closure to ensure effective inflammation and maintenance of epithelial integrity. Curr Biol. 2022 Jul; .

Zhang J, Zhou Y, Huang T, Wu F, Liu L, Kwan JSH, Cheng ASL, Yu J, To KF, Kang W. PIEZO1 functions as a potential oncogene by promoting cell proliferation and migration in gastric carcinogenesis. Mol Carcinog. 2018; 57(9):1144–1155.

Appendix 1

Section 1. Boundary conditions of governing equation

On the Dirichlet boundaries $y = 0$ and $y = 1$ (Eq. 5), the cell density is determined by functions $g_1(x,t)$ and $g_2(x,t)$ which are continuous on $[0,1]\times[0,+\infty)$. Since both of these are randomly generated from the same approach, without loss of generality, let's say $g(x,t)$. Covering $[0,1]\times[0,+\infty)$ with a grid, taking mesh sizes h_x and h_t and labeling grid nodes $(x,t) = (x_i, t_j) = (ih_x, jh_t)$ by indices (i,j), the function values at grid points $g_{i,j} = g(x_i, t_j)$ are taken to follow a normal distribution

$$g_{i,j} \overset{iid}{\sim} \mathcal{N}(\mu_0, \sigma_0^2) \tag{24}$$

with mean μ_0 and standard deviation σ_0 ($\mu_0 = 0.6$ and $\sigma_0 = 0.3$ were adapted in the simulation). This models the variability of the influx of cells from the monolayer moving into the wound region. Thereafter, the function $g(x,t)$ is given by an interpolation on $g_{i,j}$. Specifically, the boundary conditions on $y = 0$ and $y = 1$ are classical Dirichlet boundary conditions with a constant influx μ_0 if $\sigma_0 = 0$.

Section 2. Initial condition of governing equation

Assume $u(x,y,t)$ is a function defined on $[0,1]\times[0,1]\times[0,+\infty)$ and satisfies the following diffusion equation

$$\frac{\partial u}{\partial t} = \nabla \cdot (\boldsymbol{D}\nabla u) \tag{25}$$

with the same diffusivity $\boldsymbol{D}$ as in Eq. 3 and the same boundary conditions as in Eq. 5:

$$\begin{gathered} u(x,0,t) = g_0(x,t), \quad u(x,1,t) = g_1(x,t), \\ \frac{\partial u(0,y,t)}{\partial x} = \frac{\partial u(1,y,t)}{\partial x} = 0, \end{gathered} \tag{26}$$

while the initial condition is globally zero:

$$u(x,y,0) \equiv 0. \tag{27}$$

With this setting, the wound region ($u = 0$) is narrowing down from the whole square domain $[0,1]\times[0,1]$ to a heterogeneous horizontal banded region in the middle of the domain, before finally shrinking to zero area and disappearing at $t = t_{end}$. At a certain time point $t = t_0 \in (0, t_{end})$ during this process,we set $\rho(x,y,0) = u(x,y,t_0)$ as the initial condition of our governing equation Eq. 2.

In other words, this initial condition is generated by the governing equation (Eq. 2) but without retraction, starting from zero initial values and diffusing cells without any retraction for a period of time, until retractions were introduced. This enables us to start with a variable, and more physiological, initial condition compared to taking a constant values at the wound edge. At the moment right before the first retraction, cell densities across the domain $[0,1]\times[0,1]$ are the initial values for the governing equation.

Section 3. Positive definite diffusivity

The matrix $d\cdot(w_I\boldsymbol{I} + w_A\boldsymbol{A})$ is diagonal, has a positive spectrum, thus the diffusivity $\boldsymbol{D} = d\cdot(w_I\boldsymbol{I} + w_A\boldsymbol{A})\cdot\hat{D}_\alpha(\rho)$ of governing PDE (Eq. 2) is positive definite if and only if the scalar diffusion coefficient $\hat{D}_\alpha(\rho) > 0$, which depends on the value of adhesion coefficient α. By inspecting this 5-th degree polynomial, we see that $\hat{D}_\alpha(\rho) > 0$ unconditionally holds for all levels of cell density $\rho \in (0,1)$ as long as

$$\alpha < \hat{\alpha} := \frac{1}{17 - 4\sqrt{15}} \approx \frac{2}{3}, \tag{28}$$

with a critical value $\hat{\alpha}$. When $\alpha \geq \hat{\alpha}$, there exists an interval

$$I_\alpha = \left(\frac{1+7\alpha-\sqrt{1-34\alpha+49\alpha^2}}{12\alpha}, \frac{1+7\alpha+\sqrt{1-34\alpha+49\alpha^2}}{12\alpha} \right) \tag{29}$$

such that $\hat{D}_\alpha(\rho) < 0$ if and only if $\rho \in I_\alpha$. That is, the diffusivity is negative definite when cell density $\rho \in I_\alpha$, which results in the ill-posedness of the initial value PDE problem. As $\alpha \to 1$, the interval I_α expands from a single point $17 + 4\sqrt{15} \approx 1.5$ to $I_1 = (1/3,\ 1)$.

Section 4. Retraction is modeled by advection

Performing a Taylor expansion centered at $\boldsymbol{x} = \boldsymbol{x}_{i,j}$ of the cell density ρ in the discrete master equation (Eq. 1) without specifying $b^{\rightarrow}_{i,j}$, we have

$$\frac{\partial \rho}{\partial t} = \nabla \cdot (\boldsymbol{D}\nabla\rho + h \cdot (1-\rho)(1-\alpha\rho)^3 \cdot (b^{\leftarrow} - b^{\rightarrow}, b^{\uparrow} - b^{\downarrow})^T) + \mathcal{O}(h^2) \tag{30}$$

where $\boldsymbol{D}$ is the same diffusivity as in Eq. 3. So by taking $h \to 0$, the continuum limit would be a simple diffusion equation $\partial\rho/\partial t = \nabla \cdot (\boldsymbol{D}\nabla\rho)$ without an advection term, unless both $\Delta b^{\leftrightarrow} = b^{\leftarrow} - b^{\rightarrow}$ and $\Delta b^{\updownarrow} = b^{\uparrow} - b^{\downarrow}$ are $\mathcal{O}(1/h)$, the advection scaling. Therefore, we define $b^{\rightarrow}_{i,j} := r^{\rightarrow}_{i,j}/h$ with $r^{\rightarrow}_{i,j} \in \mathcal{O}(1)$. By taking $h \to 0$ under this setting, Eq. 30 turns into our continuum limit Eq. 2, where the retraction is modeled by advection.

Section 5. Function smoothing

To localize the retraction region Eq. 17, we smooth the Heaviside function $H(\gamma - \rho)$ (Eq. 18) using a hyperbolic tangent function

$$\tilde{H}(\gamma - \rho) = \frac{1}{2} \cdot (1 + \tanh(k \cdot (\gamma - \rho))), \tag{31}$$

where k is the steepness level at transition point $\rho = \gamma$ ($k = 10$ was adapted in the simulations). On the other hand, the indicator function $\mathbb{1}_{\Omega_i}(\boldsymbol{x})$ is smoothed using a 2D generalized bell-shaped function:

$$\tilde{\mathbb{1}}_{\Omega_i}(\mathbf{x}) = \frac{1}{1 + (\frac{dist(\mathbf{x},\Omega_i)}{k_1})^{2k_2}}, \tag{32}$$

where k_1 and k_2 are parameters determining the width and steepness of the transition region in the smoothing process. The distance between a point $\mathbf{x}$ and a set Ω_i in 2D Euclidean space is induced by a natural 2-norm:

$$dist(\mathbf{x}, \Omega_i) := \inf_{\mathbf{y}\in\Omega_i} \|\mathbf{x} - \mathbf{y}\|. \tag{33}$$

Since the indicator function $\mathbb{1}_{\Omega_i}(\boldsymbol{x})$ is equivalent to its 1D form $\mathbb{1}_{[c_i-\omega_r/2, c_i+\omega_r/2]}(x)$ (Eq. 19) given the banded region Ω_i, the 2D generalized bell-shaped function $\tilde{\mathbf{1}}_{\Omega_i}(\boldsymbol{x})$ (Eq. 32) can be simplified into a 1D version:

$$\tilde{\mathbb{1}}_{[c_i-\omega_r/2, c_i+\omega_r/2]}(x) = \frac{1}{1 + \left|\frac{x-c_i}{k_1}\right|^{2k_2}}. \tag{34}$$

Section 6. Model dimensionalization

Recall that Eq. 1 is our non-dimensional master equation with the transitional probability Eq. 12. In order to relate the dimensions in the model to the experiments, we take the dimensional variables to be (1) $\hat{\rho}_{i,j} := \rho_{\max} \cdot \rho_{i,j}$ ($\rho_{\max}$ is the maximal cell density), (2) $\hat{h} := l \cdot h$ (l is the characteristic length) and (3) $\hat{t} := \lambda^{-1} \cdot t$ (λ^{-1} is the characteristic time). Hence, the dimensional transitional probability becomes

$$\hat{T}^{\rightarrow}_{i,j} = (1 - \frac{\hat{\rho}_{i+1,j}}{\rho_{max}})(1 - \alpha\frac{\hat{\rho}_{i-1,j}}{\rho_{max}})(1 - \alpha\frac{\hat{\rho}_{i,j+1}}{\rho_{max}})(1 - \alpha\frac{\hat{\rho}_{i,j-1}}{\rho_{max}})(d^{\leftrightarrow} \cdot \frac{\hat{\rho}_{i,j}}{\rho_{max}} \cdot \frac{l^2}{\hat{h}^2} + r^{\rightarrow}_{i,j} \cdot \frac{l}{\hat{h}}) \tag{35}$$

which can be taken into the master equation (Eq. 1) with the dimensional time derivative

$$\frac{\partial \rho}{\partial t} = \frac{\partial(\frac{\hat{\rho}}{\rho_{max}})}{\lambda \hat{t}} = \frac{1}{\lambda \rho_{max}} \cdot \frac{\partial \hat{\rho}}{\partial \hat{t}}, \tag{36}$$

and obtain the continuum limit by taking $\hat{h} \to 0$:

$$\frac{\partial \hat{\rho}}{\partial \hat{t}} = \nabla \cdot (\tilde{\boldsymbol{D}} \nabla \hat{\rho}) + \nabla \cdot (\tilde{\boldsymbol{R}} \hat{\rho}) \tag{37}$$

where $\tilde{\boldsymbol{D}}$ is the dimensional diffusivity (diffusion coefficient) given by:

$$\tilde{\boldsymbol{D}} = \frac{\lambda l^2}{\rho_{max}^5} \cdot d \cdot (w_I \boldsymbol{I} + w_A \boldsymbol{A}) \cdot \tilde{D}_\alpha(\hat{\rho}) \tag{38}$$

with

$$\tilde{D}_\alpha(\hat{\rho}) = 2\rho_{max}^4 \hat{\rho} - (1 + 11\alpha)\rho_{max}^3 \hat{\rho}^2 + (8\alpha + 16\alpha^2)\rho_{max}^2 \hat{\rho}^3 - (13\alpha^2 + 7\alpha^3)\rho_{max} \hat{\rho}^4 + 6\alpha^3 \hat{\rho}^5 \tag{39}$$

and $\boldsymbol{I} = \boldsymbol{I}_2$, $\boldsymbol{A} = diag(0, 1)$ are defined as before in Eq. 3. On the other hand, $\tilde{\boldsymbol{R}}$ is the dimensionalized retraction (advection velocity) given by

$$\tilde{\boldsymbol{R}} = \frac{\lambda l}{\rho_{max}^4} \cdot (\rho_{max} - \hat{\rho})(\rho_{max} - \alpha \hat{\rho})^3 \cdot (\Delta r^{\leftrightarrow}, \Delta r^{\updownarrow})^T \in \mathbb{R}^2 \tag{40}$$

where $\Delta r^{\leftrightarrow}$ and $\Delta r^{\updownarrow}$ are defined as in Eq. 17.

In order to connect the model with the experiments and to calculate the effective cell diffusion coefficient as well as the advection velocity, we need to know the 3 parameters: λ, l and $\rho_{\max}$. We notice that $\lambda l^2 = v \cdot l$, where $v := \lambda l$ is actually the characteristic velocity (length over time). Hence, if we have a measurement of the characteristic velocity and the length scale, we can determine the characteristic time by $\lambda = v/l$. In conclusion, we can connect our theory and numerical parameters with the biological experiments in the following way:

- Maximal cell density $\rho_{\max}$ and cell density ρ: here ρ is interpreted as a number density, i.e., $\rho dxdy$ is the number of individuals with the position in the phase area $dxdy$ centered at (x, y). We can quantify this from the experimental results: put down a grid, count the number of cells in each single square and get a spatial representation of the cell density. In the monolayer region away from the front edge, we expect the cell density should be nearly uniform spatially and temporally, and that value could be used for $\rho_{\max}$.
- Characteristic length l: we define the characteristic length scale to be the distance from the wound edge to the region where the cells reach the maximal density in the monolayer. In our numerical tests, we did not simulate the whole experimental domain, instead, our simulation focused on the region of transition, that is, the region in which the cell density transits from the front to the maximum.
- Characteristic velocity v: the velocity of the moving front can be used for this, by averaging the front advancing speed measured by cell shape analysis.
- Characteristic time λ^{-1}: since we already have the way to determine the characteristic length l and velocity v, the characteristic time can be derived directly by $\lambda^{-1} = l/v$.

With the measurements mentioned above, we are able to calculate $\rho_{\max}$, l, v, λ and hence the diffusion coefficient and retraction velocity. At this point, we do not have a direct measurement for the adhesion coefficient α. A direct measurement for the cell-cell adhesion is being considered in our future work.

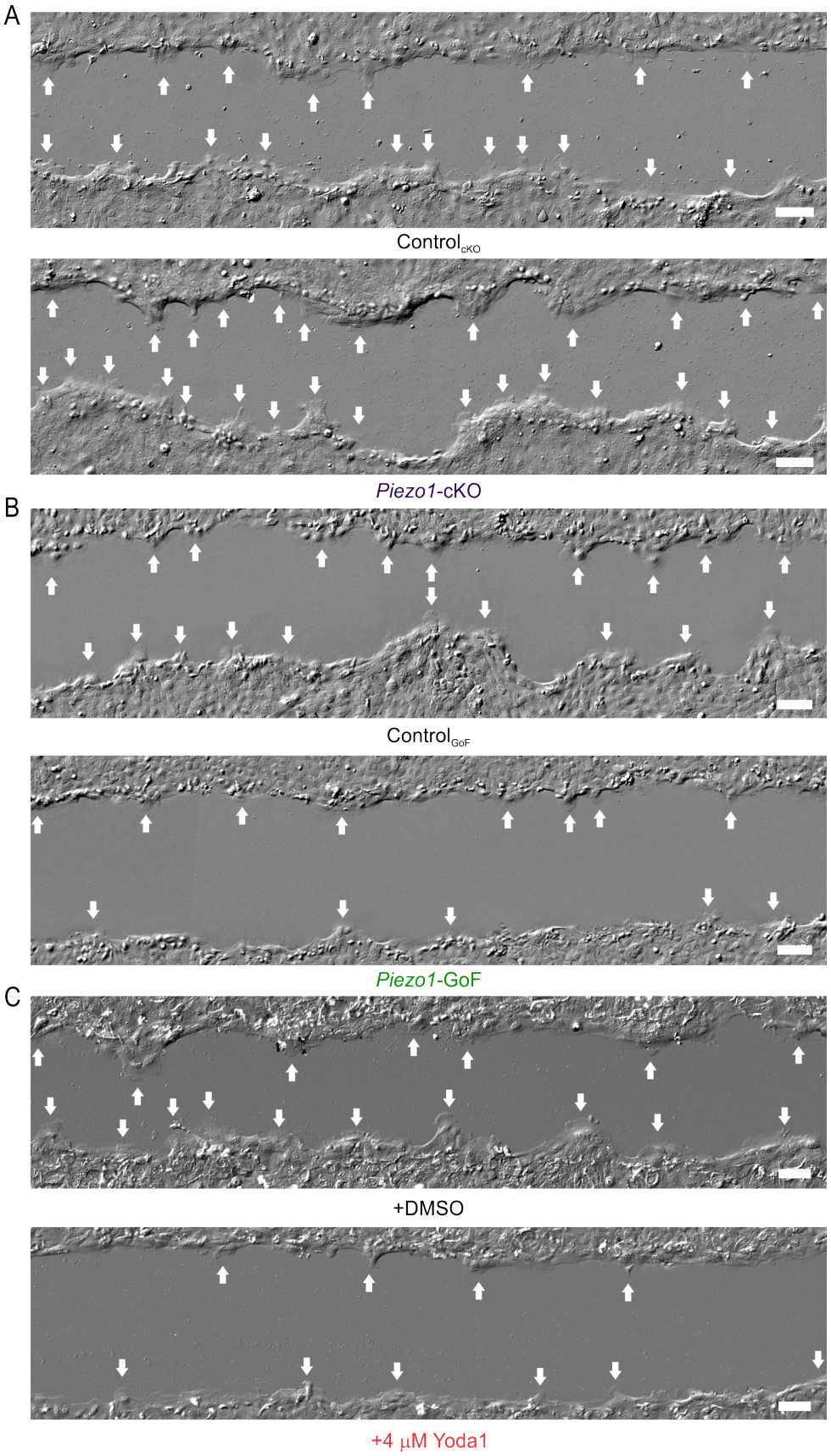

Figure 1—figure supplement 1. PIEZO1 inhibits leader cell formation at wound margins. Representative DIC images of wounds generated in (**A**; *top*) Control$_{cKO}$, (**A**; *bottom*) *Piezo1*-cKO, (**B**; *top*) Control$_{GoF}$, (**B**; *bottom*) *Piezo1*-GoF, (**C**; *top*) DMSO-treated and (**C**; *bottom*) 4 μM Yoda1-treated monolayers. White arrows indicate leader cell protrusions. Representative images were taken at the same time point as the respective control field of view. Scale bar = 100 μm. Related to ***Figure 1***.

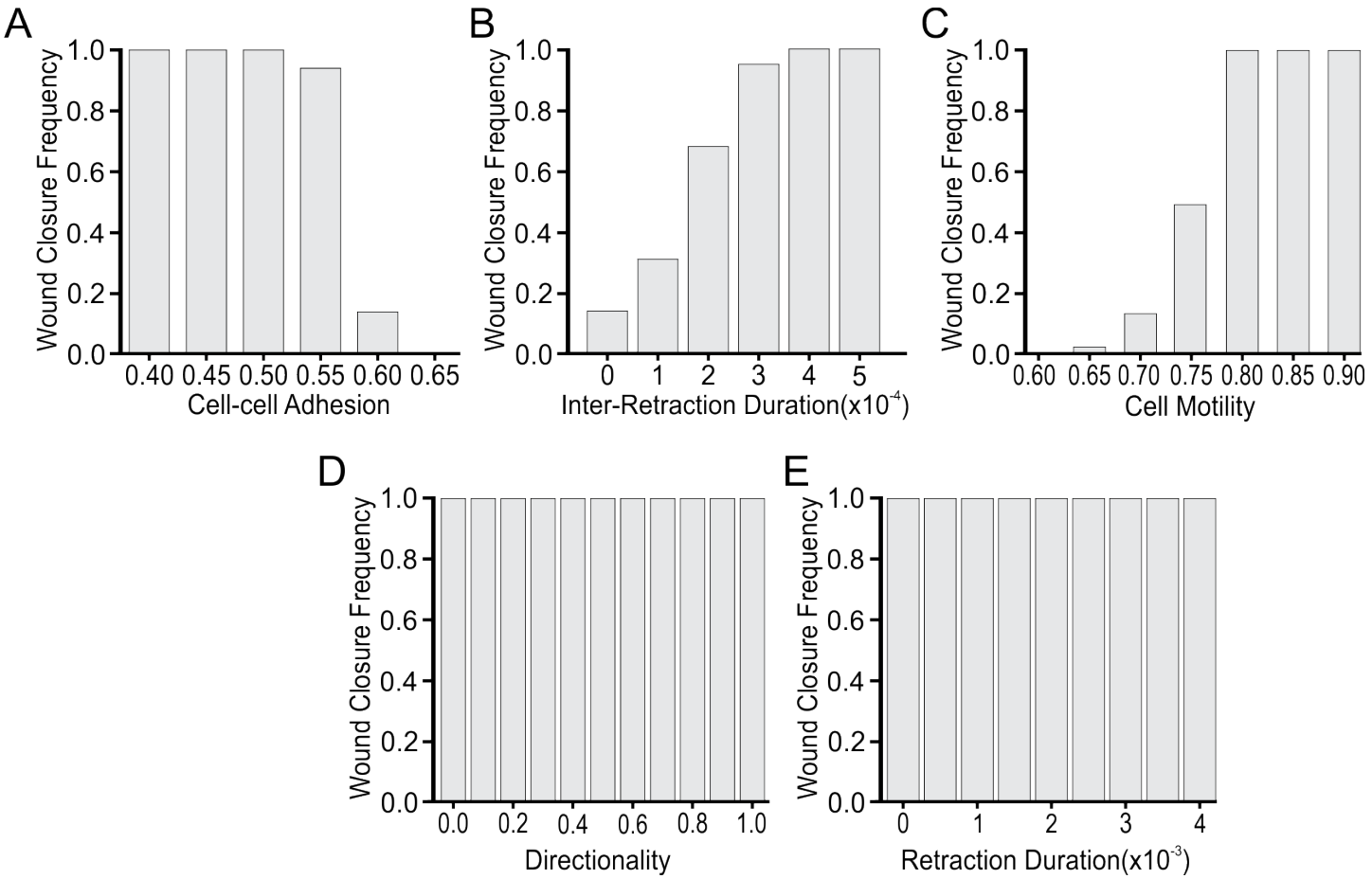

Figure 2—figure supplement 1. Wounds fail to reach closure if parameter values exceed reasonable ranges. (A) The percentage of wound closure cases under different levels of cell-cell adhesion. **(B, C, D, E)** Similar to (A) but for inter-retraction duration, cell motility, directionality and retraction duration respectively. Related to ***Figure 2F***.

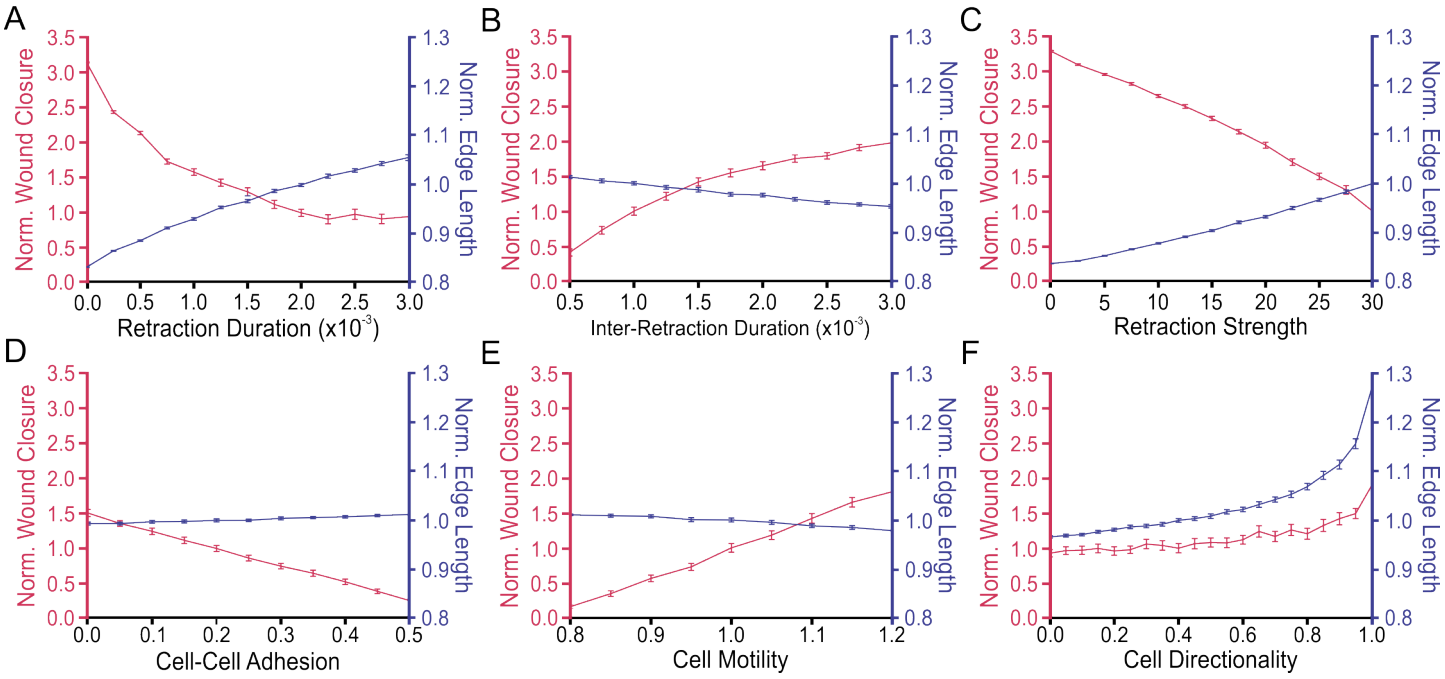

Figure 2—figure supplement 2. Cell Directionality is the only parameter which replicates all experimental results. (A) The mean of 100 simulation results showing the effect of retraction duration on normalized wound closure (*red; left axes*) and edge length (*blue; right axes*). Error bars depict the standard error of mean. **(B-F)** Similar to (A) but for inter-retraction duration, retraction strength, cell-cell adhesion, cell motility and directionality, respectively. The data in C and F are also shown in Fig. 2G and 2H but are reproduced here for ease of comparison.

	retraction duration (min)	inter-retraction duration (min)	retraction strength ($\mu m/min$)
	mean, sem	mean, sem	mean, sem
Control$_{cKO}$/ DMSO-treated	4.63, 2.16	2.19, 0.81	1.85, 0.47
Piezo1-cKO	6.00, 1.77	6.45, 2.74	0.88, 0.14
Yoda1-treated	0.76, 0.07	0.90, 0.08	5.31, 0.93
Control$_{GoF}$	0.91, 0.11	1.86, 0.50	0.99, 0.10
Pieoz1-GoF	1.07, 0.17	0.94, 0.14	1.62, 0.19

	cell motility ($\mu m/min$)
	mean, sem
Control$_{cKO}$	0.56, 0.04
Piezo1-cKO	0.78, 0.08
DMSO-treated	0.46, 0.03
Yoda1-treated	0.48, 0.03
Control$_{GoF}$	1.28, 0.08
Piezo1-GoF	1.09, 0.06

Figure 3—figure supplement 1. PIEZO1 activity affects single cell migration. Mean and standard error of mean (sem) of single cell migration dataset (retraction duration, inter-retraction duration, retraction strength and cell motility) under different experimental conditions. Retraction duration data was derived by kymograph measurements, retraction strength derived from cell shape analysis and cell motility data from tracking cells during single cell migration assays (***Holt et al.*** (***2021***)).

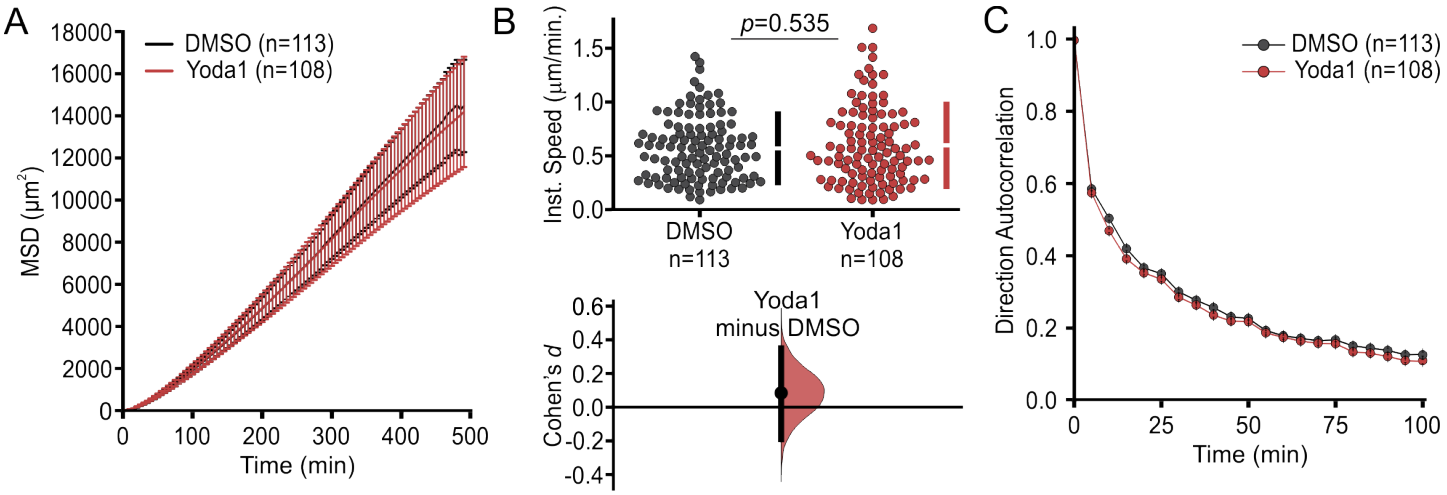

Figure 3—figure supplement 2. Yoda1 has no effect on single cell migration. (A) Mean Squared Displacement (MSD) analysis of Yoda1-treated keratinocytes. Average MSD plotted as a function of time. **(B)** Cumming plot illustrating quantification of the average instantaneous speed from tracked individual Yoda1-treated keratinocytes plotted against DMSO Control (Cohen's *d* = 0.0843; *p* value calculated via two-sample t-test). **(C)** Average direction autocorrelation of Yoda1-treated keratinocytes relative to DMSO-treated control cells plotted as a function of time. *n* in A-C denotes the number of tracked individually migrating keratinocytes for each condition. Related to ***Table 2***; ***Figure 3—figure Supplement 1***.

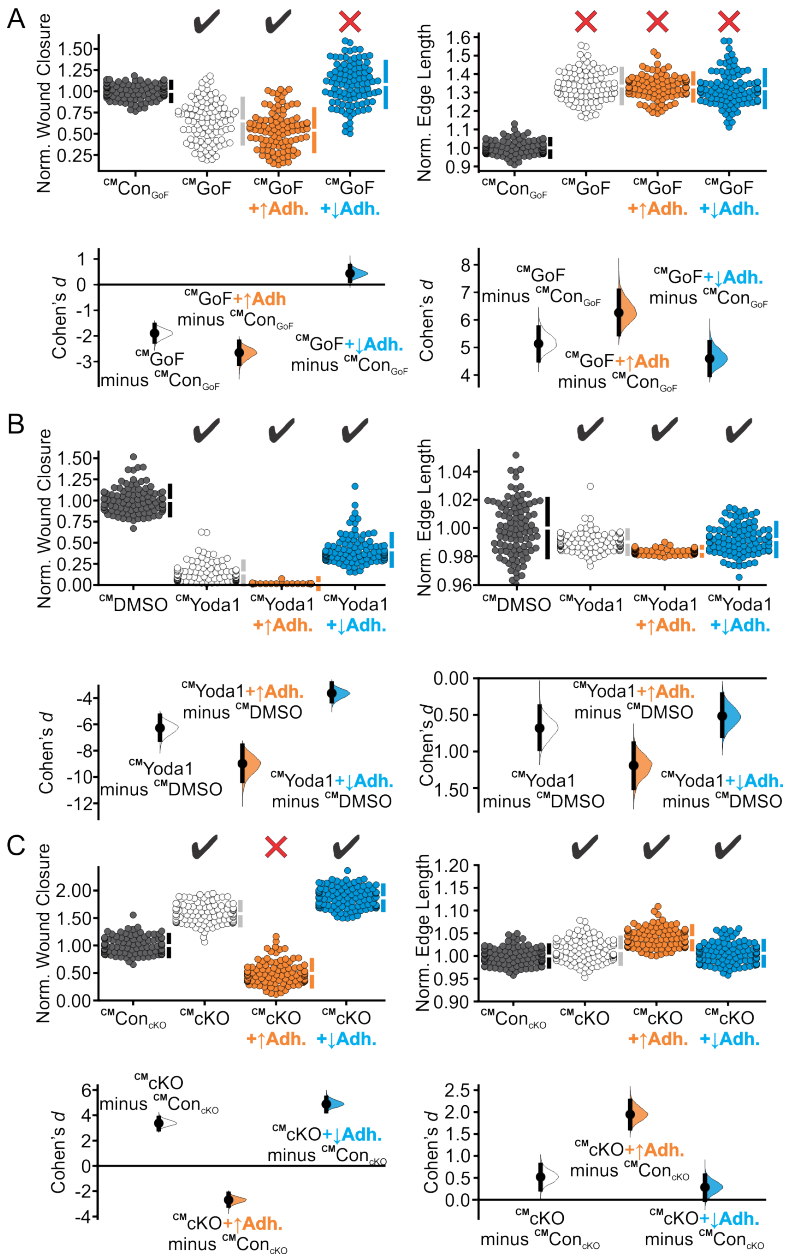

Figure 3—figure supplement 3. Varying cell-cell adhesion fails to match all the experimental trends. (A) Cumming plots showing simulation results in which we use our calibrated model (^{CM}) to predict how PIEZO1 affects wound closure (*left column*) and wound edge length (*right column*) in simulated Control$_{GoF}$ monolayers (*gray*), *Piezo1*-GoF monolayers without altered adhesion parameters (*white*), *Piezo1*-GoF monolayers with increased cell-cell adhesion (*orange)* and decreased cell-cell adhesion (*blue)* **(B)** Similar to A but using simulation results from DMSO-treated monolayers (*gray*), Yoda1-treated monolayers without altered adhesion parameters (*white*), Yoda1-treated monolayers with increased cell-cell adhesion (*orange)* and decreased cell-cell adhesion (*blue)*. **(C)** Similar to C but using simulation results from Control$_{cKO}$ monolayers (*gray*), *Piezo1*-cKO monolayers without altered adhesion parameters (*white*), and *Piezo1*-cKO monolayers with increased cell-cell adhesion (*orange)* and decreased cell-cell adhesion (*blue)*. In A-C, n = 100 simulation results for each condition. To account for differences between control cases, data are normalized by rescaling to the mean of the corresponding control. Larger normalized wound closure indicates faster wound closure, while a smaller normalized wound closure indicates slower wound closure. Similarly, a larger normalized edge length indicates a more featured wound while a smaller normalized edge length indicates a flatter or less featured wound. Black check marks at the top of each plot condition indicate that simulation results match experimental trends while a red cross indicates the simulations fail to match the experiment results. Related to ***Table 3***. For comparison with experimental data see ***Figure 1B, F***.

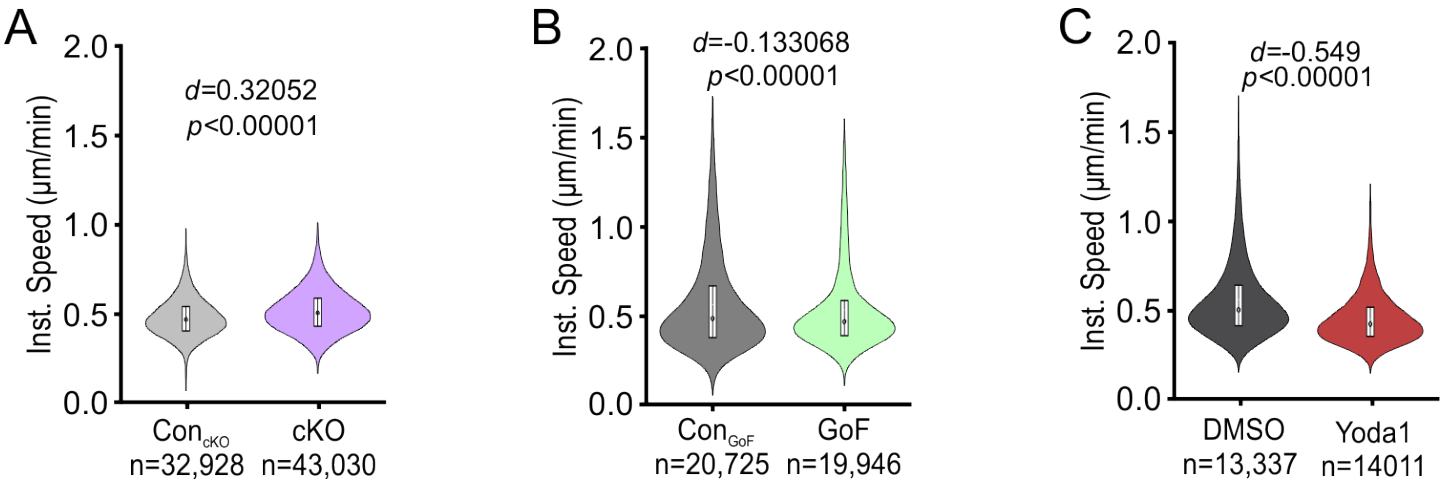

Figure 4—figure supplement 1. PIEZO1 inhibits keratinocyte speed during collective cell migration. Violin plots quantifying the average instantaneous cell speed of tracked cells in **(A)** Control_{cKO} vs. *Piezo1*-cKO, **(B)** Control_{GoF} vs. *Piezo1*-GoF, and **(C)** DMSO and 4 μM Yoda1-treated keratinocytes monolayers. For A-C, *p* value calculated via Mann-Whitney Test. For A-C, n denotes the number of individual cell trajectories. See also ***Figure 4***.

Condition:	Con_{cKO}	cKO	Con_{GoF}	GoF	DMSO	Yoda1
Length Constant :	81.2012 μm	102.673 μm	235.135 μm	149.595 μm	174.775 μm	116.216 μm

Figure 5—figure supplement 1. PIEZO1 inhibits the length scale of spatial autocorrelation in keratinocytes. Summary table showing the length constant, or the distance at which the spatial autocorrelation value is estimated to reach 0.37, for each experimental condition. Length constants were calculated by fitting a curve to the respective experimental dataset. See also ***Figure 5***.

Δr(μm)	5G *p* values:	5H *p* values:	5I *p* values:
30	4.44192×10^{-4}	8.9669×10^{-6}	–
45	6.655×10^{-4}	1.12971×10^{-5}	0.00395
60	8.20254×10^{-4}	1.2346×10^{-5}	0.00211
75	0.00117	1.68092×10^{-5}	–
90	0.00171	2.75864×10^{-5}	0.00148
105	0.00215	4.77604×10^{-5}	0.00107
120	0.00276	7.18346×10^{-5}	0.00091
135	0.00317	1.38902×10^{-4}	0.00124
150	0.00333	2.80603×10^{-4}	0.00107
165	0.00398	4.54668×10^{-4}	0.00152
180	0.0033	7.97585×10^{-4}	0.00133
195	0.00376	0.00141	0.00127
210	0.00425	0.00226	0.00161
225	0.00437	0.00437	0.00181
240	0.00389	0.00457	0.00163
255	0.0039	0.00763	0.00271
270	0.00419	0.0132	0.00252
285	0.00367	0.01619	0.00289
300	0.00291	0.01768	0.00471
315	0.00304	0.02339	0.00519
330	0.00385	0.03248	0.00634
345	0.00234	0.03299	0.0087
360	0.00259	0.02911	0.00775
375	0.0025	0.04128	0.01328
390	0.00322	0.07233	0.01261
405	0.00267	0.03511	0.01511
420	0.00286	0.04792	0.01983

Figure 5—figure supplement 2. Specific *p* values for plotted points seen in Figure 5 H-J.

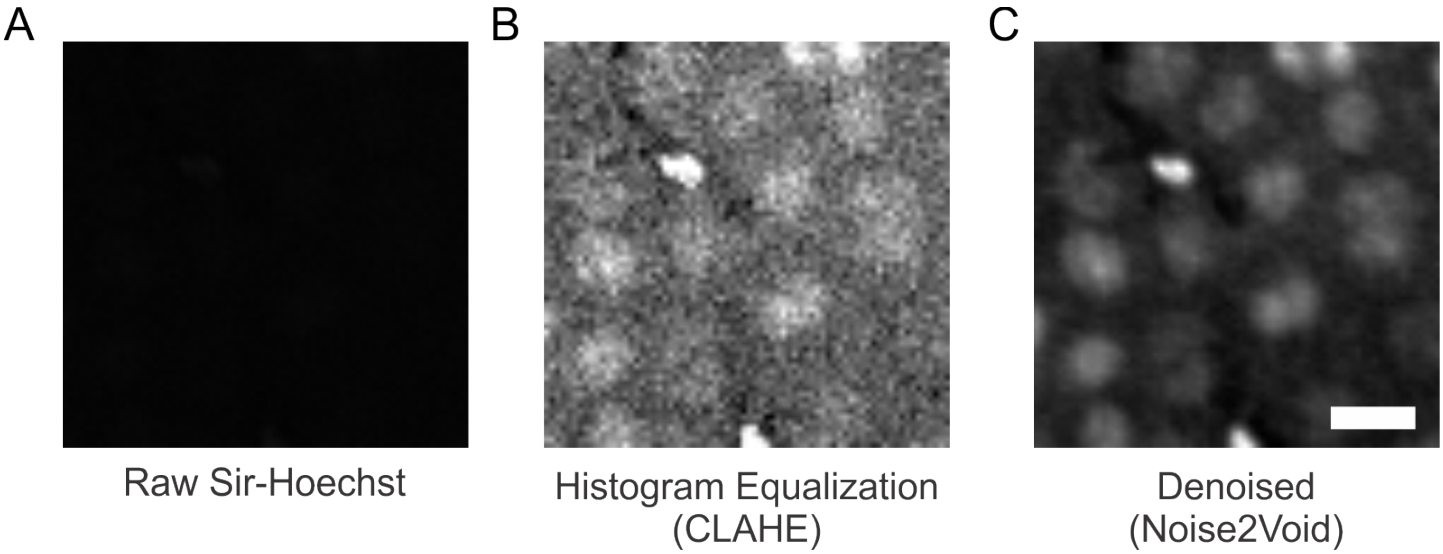

Figure 6—figure supplement 1. Image processing pipeline for nuclei images. Representative images of processing steps to boost signal-to-noise ratio of **(A)** raw Sir-Hoechst images by first performing **(B)** histogram equalization using Contrast Limited Adaptive Histogram Equalization (CLAHE). **(C)** For some images, the denoising algorithm Noise2Void was used to further increase the signal-to-noise ratio of nuclei. Note: all images adjusted to the same brightness and contrast settings. Scale bar = 20 μm.